



The Similarity of Abundance Ratio Trends and Nucleosynthetic Patterns in the Milky Way Disk and Bulge

Emily Griffith¹ , David H. Weinberg¹ , Jennifer A. Johnson¹ , Rachael Beaton² , D. A. García-Hernández^{3,4} , Sten Hasselquist^{5,12} , Jon Holtzman⁶ , James W. Johnson¹ , Henrik Jönsson^{7,8} , Richard R. Lane⁹, David M. Nataf¹⁰ , and Alexandre Roman-Lopes¹¹

¹ The Department of Astronomy and Center of Cosmology and AstroParticle Physics, The Ohio State University, Columbus, OH 43210, USA; griffith.802@osu.edu

² The Carnegie Observatories, 813 Santa Barbara Street, Pasadena, CA 91101, USA

³ Instituto de Astrofísica de Canarias (IAC), E-38205 La Laguna, Tenerife, Spain

⁴ Universidad de La Laguna (ULL), Departamento de Astrofísica, E-38206 La Laguna, Tenerife, Spain

⁵ Department of Physics & Astronomy, University of Utah, Salt Lake City, UT 84112, USA

⁶ Department of Astronomy, New Mexico State University, Las Cruces, NM 88003, USA

⁷ Materials Science and Applied Mathematics, Malmö University, SE-205 06 Malmö, Sweden

⁸ Lund Observatory, Department of Astronomy and Theoretical Physics, Lund University, Box 43, SE-22100 Lund, Sweden

⁹ Instituto de Astronomía y Ciencias Planetarias de Atacama, Universidad de Atacama, Copayapu 485, Copiapó, Chile

¹⁰ Center for Astrophysical Sciences and Department of Physics and Astronomy, The Johns Hopkins University, Baltimore, MD 21218, USA

¹¹ Departamento de Astronomía, Universidad de La Serena—Av. Juan Cisternas, 1200 North, La Serena, Chile

Received 2020 September 10; revised 2020 December 21; accepted 2020 December 22; published 2021 March 8

Abstract

We compare abundance ratio trends in a sample of $\sim 11,000$ Milky Way bulge stars ($R_{GC} < 3$ kpc) from the Apache Point Observatory Galactic Evolution Experiment (APOGEE) to those of APOGEE stars in the Galactic disk (5 kpc $< R_{GC} < 11$ kpc). We divide each sample into low-Ia (high-[Mg/Fe]) and high-Ia (low-[Mg/Fe]) populations, and in each population, we examine the median trends of [X/Mg] versus [Mg/H] for elements $X = \text{Fe, O, Na, Al, Si, P, S, K, Ca, V, Cr, Mn, Co, Ni, Cu, and Ce}$. To remove small systematic trends of APOGEE abundances with stellar $\log(g)$, we resample the disk stars to match the $\log(g)$ distributions of the bulge data. After doing so, we find nearly identical median trends for low-Ia disk and bulge stars for all elements. High-Ia trends are similar for most elements, with noticeable (0.05–0.1 dex) differences for Mn, Na, and Co. The close agreement of abundance trends (with typical differences $\lesssim 0.03$ dex) implies that similar nucleosynthetic processes enriched bulge and disk stars despite the different star formation histories and physical conditions of these regions. For example, we infer that differences in the high-mass slope of the stellar initial mass function between disk and bulge must have been $\lesssim 0.30$. This agreement, and the generally small scatter about the median sequences, means that one can predict all of a bulge star’s APOGEE abundances with good accuracy knowing only its measured [Mg/Fe] and [Mg/H] and the observed trends of disk stars.

Unified Astronomy Thesaurus concepts: [Nucleosynthesis \(1131\)](#); [Explosive nucleosynthesis \(503\)](#); [Stellar nucleosynthesis \(1616\)](#); [Chemical abundances \(224\)](#); [Galactic abundances \(2002\)](#); [Stellar abundances \(1577\)](#); [Galactic bulge \(2041\)](#)

1. Introduction

To paint a complete picture of our Galactic enrichment history, we need to study the chemical fingerprints of stars from the outer edges to the inner depths of the Milky Way. Large-scale Galactic surveys like GALAH¹³ (De Silva et al. 2015; Martell et al. 2017), Gaia-ESO (Gilmore et al. 2012), and APOGEE¹⁴ (Blanton et al. 2017; Majewski et al. 2017) give us the power to study stellar populations throughout vast regions of the Milky Way. Each provides a glimpse of the past and unveils the chemical makeup of the interstellar medium in which the stars were born. Using APOGEE data, Hayden et al. (2015) and Nidever et al. (2015) showed that stellar populations follow the same trends in $[\alpha/\text{Fe}]$ versus $[\text{Fe}/\text{H}]$ throughout the Milky Way disk, though the distribution of stars along these tracks depends strongly on galactocentric radius R_{GC} and midplane distance $|Z|$. Extending these results, Weinberg et al. (2019, hereafter W19) found that the median

trends of [X/Mg] versus [Mg/H] for all APOGEE elements are independent of Galactic location, suggesting universality in the nucleosynthetic processes that determine these abundance ratios. In this work, we aim to extend their conclusions to the Galactic bulge by leveraging the extensive bulge coverage of APOGEE sixteenth data release (DR16) to study its stellar chemical abundances.

In addition to these large-scale programs, many groups have observed smaller ($\lesssim 100$ stars) samples of the inner Galaxy and debated their chemical similarity to the disk. Works such as McWilliam & Rich (1994; 12 giants), Cunha & Smith (2006; seven giants), Fulbright et al. (2007; 27 giants), and Lecureur et al. (2007; 53 giants) found enhancements in the bulge α -element abundances relative to disk samples.¹⁵ However, subsequent work by Meléndez et al. (2008; 20 giants) found bulge [O/Fe] values in line with their thick disk sample. More recently, the bulge/disk chemical similarities/differences have been examined by studies of both giant (e.g., Johnson et al. 2014;

¹² NSF Astronomy and Astrophysics Postdoctoral Fellow.

¹³ GALactic Archaeology with HERMES.

¹⁴ APOGEE = Apache Point Observatory Galactic Evolution Experiment, currently a part of SDSS-IV.

¹⁵ The α -elements, such as O, Mg, and Si, are produced mainly by CCSNe, while iron-peak elements in stars with solar $[\alpha/\text{Fe}] = 0$ have roughly equal contributions from CCSNe and SNe Ia.

Jönsson et al. 2017; Duong et al. 2019a, 2019b; Forsberg et al. 2019; Lomaeva et al. 2019) and dwarf (e.g., Bensby et al. 2013, 2017) stars. These works span α -elements to neutron-capture elements and include all those observed by APOGEE. Within these works, small differences between the bulge and thick disk $[X/Fe]$ versus $[Fe/H]$ median abundance trends or abundance distributions are found (see above citations). We note that the collective studies do not come to a consensus on bulge/thick disk abundance differences.

Large-scale surveys such as APOGEE can provide more substantial bulge coverage than these smaller studies. While the number of APOGEE bulge observations drastically increased with the inclusion of DR16 data (Ahumada et al. 2020), the bulge has been studied in prior data releases as well. Zasowski et al. (2019) presented $[X/Fe]$ versus $[Fe/H]$ abundance distributions and median trends of 4000 bulge stars ($R_{GC} < 4$ kpc) using DR14. They compared bulge median trends with a solar radius population, finding good agreement with their high- α population but not their low- α stars, especially at low $[Fe/H]$. APOGEE observations of 424 bulge stars through Baade’s window agree with prior bulge works, suggesting that APOGEE DR13 data do not suffer systematic biases in the bulge (Schultheis et al. 2017).

All of the prior studies cited here present bulge abundances in $[X/Fe]$ versus $[Fe/H]$ space and generally treat the bulge as a single population, comparable to the thick disk. It is well known that stellar populations at the solar annulus show two distinct trends in $[\alpha/Fe]$ versus $[Fe/H]$ space (Fuhrmann 1998; Prochaska et al. 2000; Bensby et al. 2003). These are commonly referred to as the high- α and low- α populations, though in this paper we will refer to them as low- and high-Ia, respectively, since the prephysical differences between them arise from the Type Ia supernova (SN Ia) contribution to their iron abundances. While some studies (e.g., Jönsson et al. 2017; Zasowski et al. 2019) do identify high- and low-Ia stars, the bimodality of $[\alpha/Fe]$ is less evident in the bulge, so most studies have treated the bulge as a single evolutionary sequence. When the number of stars is small, the two populations blur together. However, a recent analysis of APOGEE DR14 bulge ($R < 3.5$ kpc) stars by Rojas-Arriagada et al. (2019) found the $[Mg/Fe]$ distribution to be bimodal for stars near solar $[Fe/H]$, with a distinct low- $[Mg/Fe]$ (high-Ia) sequence that had been previously categorized as a continuation of the low-Ia population. Other recent works with APOGEE DR16 data confirm that the bulge exhibits a disklike double sequence (e.g., Bovy et al. 2019; Lian et al. 2020; Queiroz et al. 2020).

Stellar populations that span high- to low- $[Mg/Fe]$ can be decomposed into high- and low-Ia components, as in W19. Unlike prior bulge studies, we can now leverage the large bulge population observed by APOGEE DR16 to separately study the high- and low-Ia populations of the inner Galaxy. When viewed in $[X/Mg]$ versus $[Mg/H]$ space, these two populations inform us on the relative contribution of core-collapse SNe (CCSNe) and SNe Ia. Elements dominantly produced by prompt CCSN enrichment (e.g., O, Mg, Si, Ca) will display high- and low-Ia sequences with little separation, while elements with an increased SNe Ia contribution (e.g., Fe, Ni, Mn) will show a larger sequence separation. The two-process decomposition model developed by W19 allows us to quantify the relative prompt and delayed contribution to each element. By studying the abundances in Mg space rather than Fe space, we can conduct a clearer comparison of the nucleosynthetic contributions to the bulge and disk than has been done before, since Mg comes almost entirely from CCSNe.

Using APOGEE DR14 disk stars, W19 showed that the median trends of $[X/Mg]$ versus $[Mg/H]$ for the low- and high-Ia populations remained constant throughout the disk for O, Na, Mg, Al, Si, P, S, K, Ca, V, Cr, Mn, Fe, Co, and Ni. Griffith et al. (2019, hereafter GJW) expanded this work to many new elements in GALAH and drew similar conclusions. In this paper, we use APOGEE DR16 data to carry out a similar analysis of the bulge. Previous bulge studies have focused mostly on the distribution of stars in $[Fe/H]$, $[\alpha/Fe]$, or other element ratios. These distributions are sensitive to many aspects of chemical evolution, such as star formation history, star formation efficiency, and outflows. Here we focus on the median trends of $[X/Mg]$ versus $[Mg/H]$, which are sensitive mainly to the relative nucleosynthetic yields of these elements (see W19). Comparing disk and bulge sequences therefore allows us to ask whether the SNe that enriched the bulge are similar to the SNe that enriched the disk, even if the relative contributions of CCSNe and SNe Ia are different.

After discussing our data selection in Section 2, we present the APOGEE DR16 bulge abundances in Mg and Fe space in Section 3. Here we also construct a comparison disk sample and analyze the similarities and differences between the bulge and disk median high- and low-Ia trends. In Section 4, we review the two-process model of W19, apply it to the disk trends, and predict the bulge abundances based on the best-fit parameters. Section 5 contains a discussion of potential constraints on the initial mass function (IMF) difference between the bulge and the disk. We summarize our work in Section 6.

2. Data

In this paper, we use data from the DR16 data set of the Sloan Digital Sky Survey (SDSS) APOGEE survey (Ahumada et al. 2020; Jönsson et al. 2020, hereafter J20). The DR16 data set extends APOGEE’s Galactic view to the southern hemisphere, as we observe with two nearly identical, 300 fiber APOGEE spectrographs (Wilson et al. 2019) on the 2.5 m Sloan Foundation telescope (Gunn et al. 2006) at Apache Point Observatory (APO) in New Mexico and the 2.5 m du Pont telescope (Bowen & Vaughan 1973) at Las Campanas Observatory (LCO) in Chile. The addition of LCO allows APOGEE to observe a greater number of stars in the inner Galaxy, crucial for the work done in this paper. Targeting selection for APOGEE-2 is described by Zasowski et al. (2017) and updated in F. Santana et al. (2021, in preparation). Bulge stars are selected as a part of the main APOGEE red giant sample. The APOGEE data are reduced as described by Nidever et al. (2015) and fed into the APOGEE Stellar Parameters and Chemical Abundances Pipeline (ASPCAP; Holtzman et al. 2015, 2018; García Pérez et al. 2016). ASPCAP returns the best-fit effective temperatures, surface gravities, and elemental abundances employed in this paper. See J20 and references therein for a more detailed description of the DR16 data reduction analysis and validation.

We use data from an internal data release including observations through 2019 November rather than the public DR16. These additional observations have been processed with the same DR16 pipeline, so we will call this data set DR16+. ¹⁶ The 4 months of additional observations add many more bulge fields, increasing the number of stars in our bulge population from 6978 in DR16 to 11,229 in DR16+. The additional data and their ASPCAP analysis will be included in APOGEE

¹⁶ APOGEE allStar file allStar-r13-133-58814.

DR17 (planned for mid-2021). We have repeated our analysis with the smaller DR16 data set and find very similar results. The DR16+ data set provides more robust median trends for difficult-to-observe elements (e.g., Na, K, Mn, Cu, Ce) and the less populated, low-metallicity regime.

We apply quality cuts to the DR16+ APOGEE catalog to extract stars with reliable, calibrated abundance measurements. We cut all stars with flags set for many bad pixels, bright neighbors, high persistence levels, broad lines, or radial velocity warnings (STARFLAGs 0, 3, 9, 16, and 17), as well as those with expected bad or dubious determinations of T_{eff} , $\log(g)$, metallicity, and α -element content (ASPCAPFLAGs 0, 3, 16, and 17). Duplicate observations are removed. We require there to be no elemental flags for [Mg/Fe] and [Fe/H] in our main sample, and we further discard stars with flagged abundances in their respective elemental analyses. After removing flagged stars, we make a signal-to-noise ratio (S/N) cut of $S/N > 100$.

Finally, we remove the cool stars by requiring $T_{\text{eff}} > 3500$ K. For some elements, cool stars produce systematic structures in [X/Fe] versus [Fe/H] space, likely due to a failure in the APSCAP fit. Our cut at 3500 K does not remove all observational artifacts, but it significantly cleans up the sample. A larger discussion of these artifacts can be found in Section 3.1 and J20.

Stars that pass these cuts span the Milky Way. While the boundaries between the disk, inner Galaxy, and bulge are debated, we define the Galactic bulge as $R_{\text{GC}} < 3$ kpc. We apply a height cut of $|Z| < 5$ kpc. We use spectrophotometric distances from Rojas-Arriagada et al. (2020) and take the Galactic center to be at 8.178 kpc (Gravity Collaboration et al. 2019). To assure that our stars reside in the inner Galaxy, we remove those with quoted distance errors greater than 10% of their distance. While we choose to use the Rojas-Arriagada et al. (2020) distances, *astroNN* (Bovy et al. 2019; Leung & Bovy 2019) and *StarHorse* (Queiroz et al. 2020) distances are also publicly available for DR16 data (see the cited papers for a more detailed comparison of methods and results). When we repeat our analysis with these two alternative distance sets, we find good agreement between the derived median abundance trends. Our results are therefore independent of the specific distance derivation used. The distribution of our bulge sample in $|Z|$ versus R_{GC} is shown in the top panel of Figure 1.

These quality and spatial cuts leave us with a sample of 11,229 stars in the bulge that have a median S/N of 149. The middle panel of Figure 1 shows the density of these stars in [Mg/Fe] versus [Fe/H] space and the distribution of their [Mg/Fe] values. We define the low-Ia population as stars that satisfy the following set of equations:

$$\begin{cases} [\text{Mg}/\text{Fe}] \geq 0.185, & [\text{Fe}/\text{H}] \leq -0.5 \\ [\text{Mg}/\text{Fe}] \geq 0.12 - 0.13[\text{Fe}/\text{H}], & -0.5 < [\text{Fe}/\text{H}] \leq 0 \\ [\text{Mg}/\text{Fe}] \geq 0.12, & [\text{Fe}/\text{H}] > 0. \end{cases} \quad (1)$$

This dividing line is plotted in Figure 1. We note that our division differs from that of W19 at $[\text{Fe}/\text{H}] \leq -0.5$, as we add a plateau to successfully separate the low-metallicity stars. We further require high-Ia stars to have $[\text{Fe}/\text{H}] > -0.5$ to avoid

contamination with the stars in the low-Ia population that scatter below $[\text{Mg}/\text{Fe}] = -0.185$ at lower metallicities. This exclusion removes 153 stars. Some excluded objects are likely true low-[Fe/H] high-Ia stars, but their low density in abundance space would not meet our criteria for median trend analysis.

While previous studies of the bulge have seen a single continuous sequence in the $[\alpha/\text{Fe}]$ versus $[\text{Fe}/\text{H}]$ plane (e.g., Ness & Freeman 2016), the histogram in Figure 1 strongly suggests the presence of two distinct populations. The distribution of [Mg/Fe] has a minimum at $[\text{Mg}/\text{Fe}] \approx 0.13$ with bimodality particularly evident near $[\text{Fe}/\text{H}] \approx 0$, as seen previously by Rojas-Arriagada et al. (2019). However, compared to the disk (see Figure 7), the high-Ia sequence is less evident at $[\text{Fe}/\text{H}] < 0$. The [Mg/Fe] distribution is affected by the height distribution of the sample (e.g., Bovy et al. 2016). Here we have not corrected for the latitude sampling bias, so our [Mg/Fe] distribution may not be representative of the full bulge population. In their study of the bulge bimodality, Lian et al. (2020) corrected this bias. After corrections, they found a stronger signal of bimodality than in the parent population. We likely see more low-Ia stars than would be representative of this Galactic region due to the higher-latitude observations. For the purposes of this paper, the separation of our sample into two populations is important mainly because it allows us to make accurate comparisons of bulge and disk populations with similar levels of SN Ia enrichment. We do not make conclusions about the relative number of stars on the low- or high-Ia sequence or the bulge metallicity distribution function (MDF), so we do not discuss the sampling bias further.

Compared to the Galactic disk (W19; Figure 1 therein), the low-Ia sequence of the bulge remains well populated to lower metallicity, though the low-Ia sequences of both the bulge and the disk reach an [Fe/H] of ~ -1.3 . The bottom panel of Figure 1 shows the median trends of the high- and low-Ia populations for the bulge and disk. Here we use the W19 disk definition ($3 \text{ kpc} < R < 15 \text{ kpc}$, $|Z| < 2 \text{ kpc}$, $1 < \log(g) < 2$, and $3700 \text{ K} < T_{\text{eff}} < 4600 \text{ K}$) but recalculate with DR16+ data and the quality cuts listed above. We will refer to this sample as the “W19 disk” throughout the paper. The [Mg/Fe] versus [Fe/H] median trends for W19 and the bulge agree to within ~ 0.05 dex at all metallicities. Agreement is further improved by matching the $\log(g)$ distributions of the disk and bulge samples as discussed below (see Section 3.3). We find that the [Mg/Fe] downturn, or knee, of both populations occurs at the same [Fe/H], in agreement with Zasowski et al. (2019).

3. Bulge Stellar Abundances

In this section, we discuss the median abundance trends of the APOGEE DR16+ bulge stars (see Tables 1 and 2). Figure 2 plots the APOGEE abundances in [X/Mg] versus [Mg/H] space for Fe, O, Na, Al, Si, P, S, K, Ca, V, Cr, Mn, Co, Ni, Cu, and Ce, along with the median trends for the high- and low-Ia populations. Median values are calculated in bins of width 0.1 dex in [Mg/H] and require >20 stars per bin. APOGEE abundances are calculated with LTE assumptions. See Osorio et al. (2020) for a discussion of the potential non-LTE (NLTE) effects on Na, Mg, K, and Ca.

While APOGEE reports C, N, and Ti for some bulge stars, we do not include them in this paper. We remove the C and N

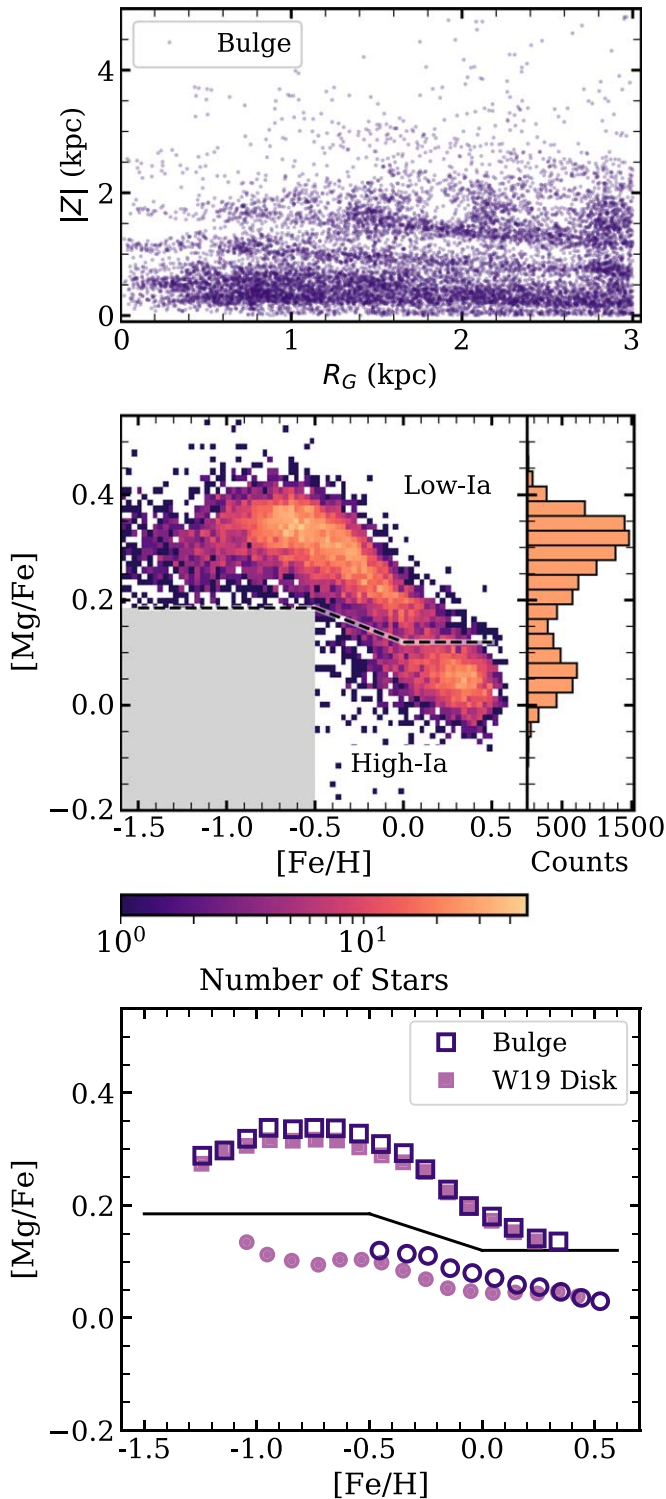


Figure 1. Top: distribution of our bulge stellar sample in the $|Z|$ vs. R_{GC} plane. Middle: density plot of stars in the bulge. The dashed line denotes our division between the high- and low-Ia populations. We exclude high-Ia stars with $[\text{Fe}/\text{H}] < -0.5$ and $[\text{Mg}/\text{Fe}] < -0.185$, located in the gray region. We include a histogram of our bulge sample’s $[\text{Mg}/\text{Fe}]$ distribution in the right panel. Bottom: median trends for the low-Ia (squares) and high-Ia (circles) bulge populations (dark purple). Those for the disk (as defined by W19) are shown in pink.

abundances, as mixing of processed material in giant stars causes the observed atmospheric abundances to differ from their birth values. We exclude Ti because the Ti I abundances

show inaccurate $[\text{Ti}/\text{Fe}]$ versus $[\text{Fe}/\text{H}]$ trends when compared to optical measurements, and Ti II abundances have excessive scatter (Hawkins et al. 2016, J20).

We further note the exclusion of some Na, K, Mn, and Ce abundances. As in previous data releases, Na remains one of the most imprecisely measured elements in DR16 with a scatter of ~ 0.1 dex (J20). As $[\text{Na}/\text{Fe}]$ errors exceed 0.1 dex at low metallicities, we cut all stars with $[\text{Fe}/\text{H}] < -0.5$ in the Na analysis. While our quality cuts remove all stars below 3500 K, ASPCAP does not report calibrated abundances for Na, K, Mn, and Ce below ~ 4000 K. Systematic trends with temperature in all four elements motivate their exclusion. Radial velocity shifts that move Ce lines into chip gaps or out of APOGEE’s wavelength range cause additional omission. After our cuts, the $[\text{Na}/\text{Mg}]$ high- and low-Ia medians still have some temperature dependence. We find that lower-temperature subsamples have higher median $[\text{Na}/\text{Mg}]$ values than higher-temperature subsamples at the same $[\text{Mg}/\text{H}]$. Appendix A further explores this temperature systematic and its influence on the median trends of Na and other elements.

The median errors on the abundance $[\text{X}/\text{Mg}]$ are comparable to those reported by Jönsson et al. (2020). We find that the median errors are $\lesssim 0.06$ dex for all elements except Ce. Errors grow (to ~ 0.1 dex) in the lower-metallicity regime for P, S, K, V, Cr, Co, and Cu. The reported abundance errors do not capture the spread in abundances about the median trends, suggesting some intrinsic abundance scatter (see Vincenzo et al. 2021 for more details). The statistical errors on the median values themselves, though, are small, as we are taking medians of hundreds of stars.

3.1. Systematics and Artifacts

Although we apply extensive quality cuts to our data, artifacts and unexpected abundance structures still appear. Most obviously, the high-Ia Cr stars split into two populations, one with higher $[\text{Cr}/\text{Mg}]$ values and one with lower. Clumps and bands can also be seen in $[\text{V}/\text{Mg}]$, $[\text{P}/\text{Mg}]$, and $[\text{Al}/\text{Mg}]$. Figure 3 plots these same data but in $[\text{X}/\text{Fe}]$ versus $[\text{Fe}/\text{H}]$ space. Here the aforementioned artifacts become more apparent, and other structures not seen in $[\text{X}/\text{Mg}]$ versus $[\text{Mg}/\text{H}]$ space pop out. We review the observed features that are caused by two broad problems in the data reduction process (J20) below.

The α finger. In the $[\text{O}/\text{Fe}]$, $[\text{Ca}/\text{Fe}]$, and $[\text{Si}/\text{Fe}]$ versus $[\text{Fe}/\text{H}]$ panels of Figure 3, a “finger” can be seen protruding from the abundance tracks. Zasowski et al. (2019) saw a similar feature in their DR14 bulge abundance distributions. The finger feature affects a small fraction of cool giants and is caused by an error on the abundance determination (J20). It is also seen in the $[\alpha/\text{M}]$ versus $[\text{M}/\text{H}]$ trends. The Si exhibits a smaller finger than O and Ca, and Mg is free of the structure. While cutting stars below 3500 K removed many of the finger stars from our analysis, the artifact still remains visible. However, due to the low number of stars in the finger, their exclusion changes the median high- and low-Ia $[\text{X}/\text{Mg}]$ trends by < 0.05 dex (see Appendix A). As such, we continue in our analysis with their inclusion. Interestingly, the finger artifact mainly plagues APOGEE bulge fields.

Cr bimodality. In both Mg and Fe space, the split in high-Ia Cr abundances is obvious. This artifact was described by J20 as the “low abundance trend” seen for some giant stars with $T_{\text{eff}} < 4000$ K, and they suggested that it comes from the TIE

Table 1
Median High-Ia (Top) and Low-Ia (Bottom) Sequences for APOGEE DR16+ α -Elements and Light-Z Elements

[Mg/H]	[O/Mg]	[Na/Mg]	[Al/Mg]	[Si/Mg]	[P/Mg]	[S/Mg]	[K/Mg]	[Ca/Mg]
-0.262	-0.044	0.002	...	-0.085	-0.018	0.022	0.025	...
-0.149	-0.017	0.019	-0.041	-0.036	-0.004	0.022	0.022	0.048
-0.043	-0.022	0.008	-0.090	-0.003	-0.018	0.014	-0.006	-0.028
0.056	-0.012	0.005	-0.044	0.013	-0.017	0.002	-0.029	-0.017
0.153	0.001	-0.003	0.012	0.025	-0.017	-0.004	-0.034	0.007
0.255	0.008	-0.010	0.081	0.026	-0.018	-0.027	-0.041	0.020
0.354	0.013	-0.020	0.170	0.023	-0.014	-0.056	-0.051	0.065
0.445	0.010	-0.030	0.230	0.019	-0.014	-0.070	-0.057	0.073
0.532	-0.000	-0.043	0.266	0.003	-0.021	-0.091	-0.069	0.094
-1.254	-0.264	-0.011	...	-0.527	-0.015	-0.190	0.231	-0.056
-1.145	-0.232	0.011	...	-0.468	0.015	-0.062	0.199	-0.005
-1.042	-0.244	0.017	...	-0.411	0.016	-0.200	0.283	-0.031
-0.95	-0.226	-0.005	...	-0.377	0.011	-0.201	0.234	-0.028
-0.844	-0.229	-0.017	...	-0.314	0.019	-0.216	0.233	-0.047
-0.746	-0.246	-0.043	...	-0.233	0.000	-0.273	0.161	-0.058
-0.646	-0.270	-0.053	...	-0.211	-0.007	-0.281	0.153	-0.079
-0.547	-0.269	-0.056	...	-0.211	-0.032	-0.266	0.110	-0.086
-0.444	-0.270	-0.056	...	-0.213	-0.066	-0.221	0.077	-0.085
-0.345	-0.274	-0.056	...	-0.165	-0.060	-0.173	0.078	-0.069
-0.248	-0.269	-0.051	-0.188	-0.128	-0.063	-0.134	0.044	-0.060
-0.149	-0.255	-0.045	-0.201	-0.096	-0.069	-0.113	0.016	-0.044
-0.049	-0.230	-0.040	-0.185	-0.062	-0.064	-0.084	-0.004	-0.036
0.046	-0.197	-0.030	-0.153	-0.040	-0.061	-0.076	-0.016	-0.028
0.142	-0.152	-0.025	-0.119	-0.017	-0.059	-0.069	-0.043	-0.030
0.241	-0.126	-0.029	-0.094	0.001	-0.060	-0.070	-0.072	-0.030
0.345	-0.103	-0.051	-0.020	-0.004	-0.056	-0.067	-0.076	0.014
0.445	-0.086	-0.071	0.024	-0.017	-0.065	-0.139	-0.106	0.019

Note. We calculate medians in bins with a width of 0.1 dex in [Mg/H], requiring >20 stars per bin. Zero-point shifts discussed in Section 4.1 are included.

Table 2
Same as Table 1 but for APOGEE DR16+ Fe-peak Elements, Cu, and Ce

[Mg/H]	[V/Mg]	[Cr/Mg]	[Mn/Mg]	[Fe/Mg]	[Co/Mg]	[Ni/Mg]	[Cu/Mg]	[Ce/Mg]
-0.262	0.015	0.001	-0.069	-0.030
-0.149	0.005	0.006	0.040	-0.200	-0.032	-0.026	-0.045	...
-0.043	-0.004	-0.012	0.020	-0.127	-0.049	-0.031	-0.032	-0.075
0.056	-0.002	-0.021	0.013	-0.063	-0.040	-0.018	-0.003	-0.070
0.153	-0.001	0.005	0.045	-0.030	-0.021	0.005	-0.013	-0.140
0.255	-0.004	0.024	0.057	0.025	0.001	0.021	0.010	-0.187
0.354	-0.009	0.041	0.068	0.082	0.032	0.051	0.057	-0.190
0.445	-0.026	0.058	0.066	0.133	0.074	0.071	0.065	-0.198
0.532	-0.041	0.072	0.052	0.145	0.106	0.082	0.105	-0.204
-1.254	-0.049	-0.001	-0.406	-0.620	-0.443	-0.247	0.169	-0.237
-1.145	-0.033	-0.052	-0.410	-0.614	-0.429	-0.254	0.151	-0.273
-1.042	-0.014	-0.114	-0.414	-0.639	-0.403	-0.248	0.142	-0.251
-0.95	-0.015	-0.171	-0.361	-0.622	-0.309	-0.230	0.097	-0.259
-0.844	-0.004	-0.166	-0.366	-0.612	-0.303	-0.216	0.047	-0.172
-0.746	-0.031	-0.154	-0.304	-0.594	-0.264	-0.210	-0.016	-0.118
-0.646	-0.056	-0.187	-0.328	-0.590	-0.268	-0.223	-0.069	-0.123
-0.547	-0.066	-0.153	-0.291	-0.566	-0.238	-0.211	-0.116	-0.181
-0.444	-0.084	-0.141	-0.270	-0.535	-0.191	-0.202	-0.121	-0.244
-0.345	-0.104	-0.168	-0.280	-0.510	-0.194	-0.203	-0.140	-0.291
-0.248	-0.114	-0.152	-0.272	-0.490	-0.164	-0.189	-0.160	-0.331
-0.149	-0.119	-0.131	-0.258	-0.443	-0.146	-0.175	-0.172	-0.333
-0.049	-0.120	-0.130	-0.242	-0.383	-0.126	-0.160	-0.166	-0.316
0.046	-0.120	-0.125	-0.219	-0.342	-0.112	-0.141	-0.164	-0.290
0.142	-0.105	-0.113	-0.197	-0.256	-0.101	-0.116	-0.126	-0.233
0.241	-0.088	-0.080	-0.183	-0.157	-0.078	-0.097	-0.087	-0.206
0.345	-0.075	-0.048	-0.174	-0.107	-0.055	-0.065	-0.092	-0.255
0.445	-0.080	-0.039	-0.134	...	-0.042	-0.043

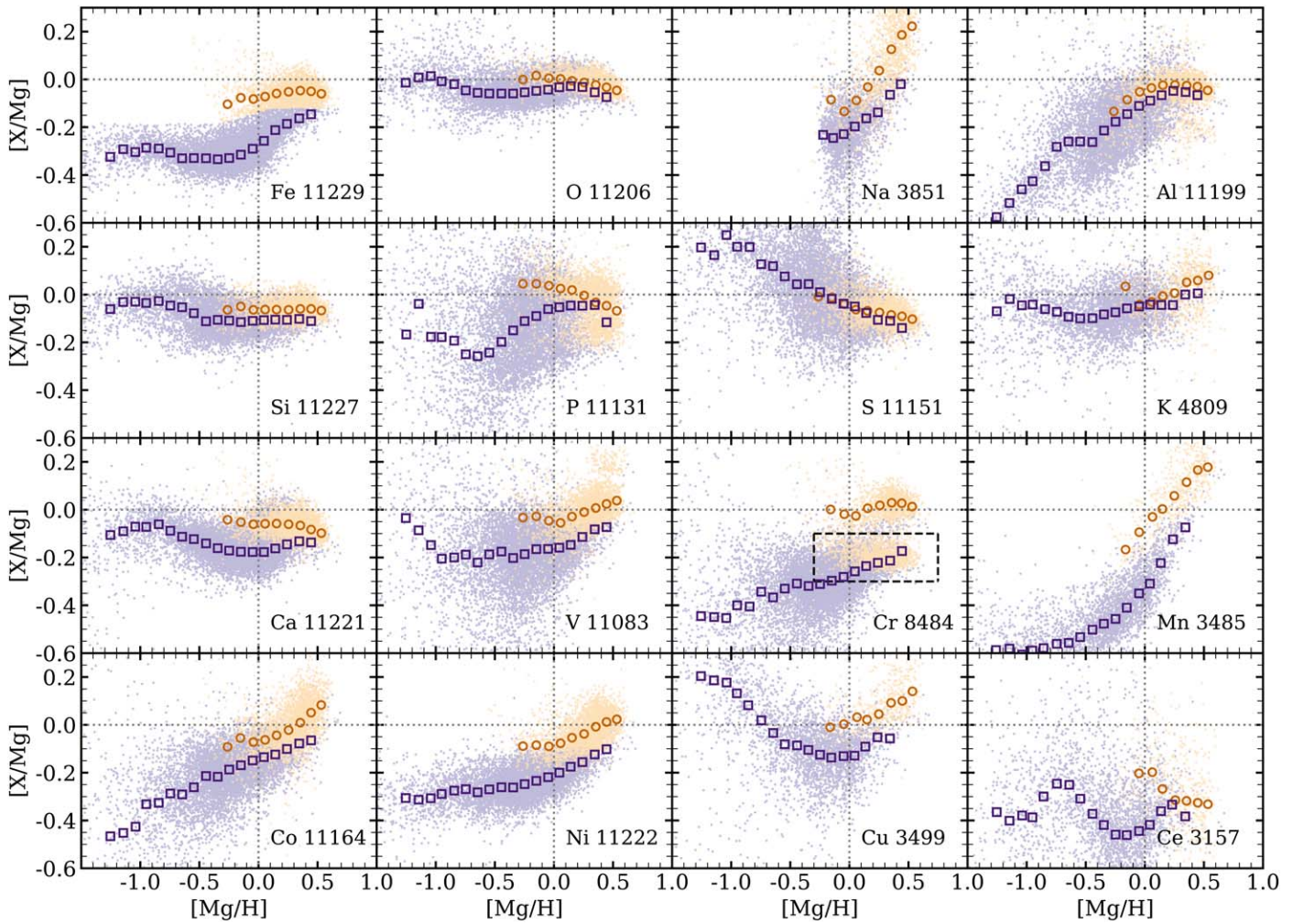


Figure 2. Bulge stellar abundance distributions in $[X/Mg]$ vs. $[Mg/H]$ space for APOGEE elements. High-Ia stars are in orange, and low-Ia stars are in purple. The medians of the high-/low-Ia populations are overplotted, where we bin by 0.1 dex and require >20 stars per bin. The dotted lines in each panel denote solar $[X/Mg]$ and $[Mg/H]$. The number in the bottom right corner of each subplot corresponds to the number of stars for each elemental population that pass our cuts. High-Ia stars with Cr abundances within the dashed box are excluded in the calculation of the high-Ia median.

option in the FERRE interpolation. While this structure affects many elements, it afflicts Cr the most. The inclusion of both groups would create a high-Ia median trend that poorly describes either one. We choose to exclude the high-Ia stars with lower $[Cr/Mg]$ from our analysis. These stars are located within the box drawn in the Cr panel of Figure 2, having $0 < [Mg/H] < 0.75$ and $-0.3 < [Cr/Mg] < -0.1$. We cut the low-Cr group because Cr trends in higher $\log(g)$ disk populations from APOGEE DR16 bear greater resemblance to the high-Cr track. Knowledge of previous works in the solar neighborhood (e.g., Bensby et al. 2014) also support this decision. The excluded stars are shown in gray in Figure 3. They have $[Fe/Mg]$ near solar, so they shift location relative on the low-Ia population, which has $[Fe/H] < 0$.

Al and P banding. In both elemental plots, the high- and low-Ia populations appear to be divided into multiple sequences or clumps. These are both instances of the low abundance trend artifacts, similar to that seen in Cr (J20). We are unable to remove or account for these systematics, as they are blended into the other features, so the abundance trends should be viewed with caution. We note that the stars within the bands are different for P, Al, and Cr.

V clump. A small cluster of high-Ia stars can be seen at higher $[V/Mg]$ and $[V/Fe]$ than the majority of the population. These stars are not the same stars in the Al or P banding. As with the α finger, the few stars in this clump have little effect on the median trend, so we do not eliminate them.

The inclusions/exclusions of stars afflicted by the artifacts discussed in this section slightly change the high- and low-Ia median sequences, with the only large impact being the high-Ia $[Cr/Mg]$ trend. For a larger discussion of the effect that these stars have on the median trends, see Appendix A. It was noted by J20 that the low abundance trends can also be seen in Ni and Co, but this structure is not apparent in our stellar selection.

3.2. Bulge Definition and Bar Influence

If the location and separation of the $[X/Mg]$ median high- and low-Ia trends differ between the bulge and the disk, implying some radial dependence, we might also expect the bulge definition to influence the observed median trends. In this paper, we take the bulge to be all stars within the cylinder defined by $R_{GC} < 3$ and $|Z| < 5$ kpc. Previous studies of the bulge and inner Galaxy have used similar, though not identical, definitions (see

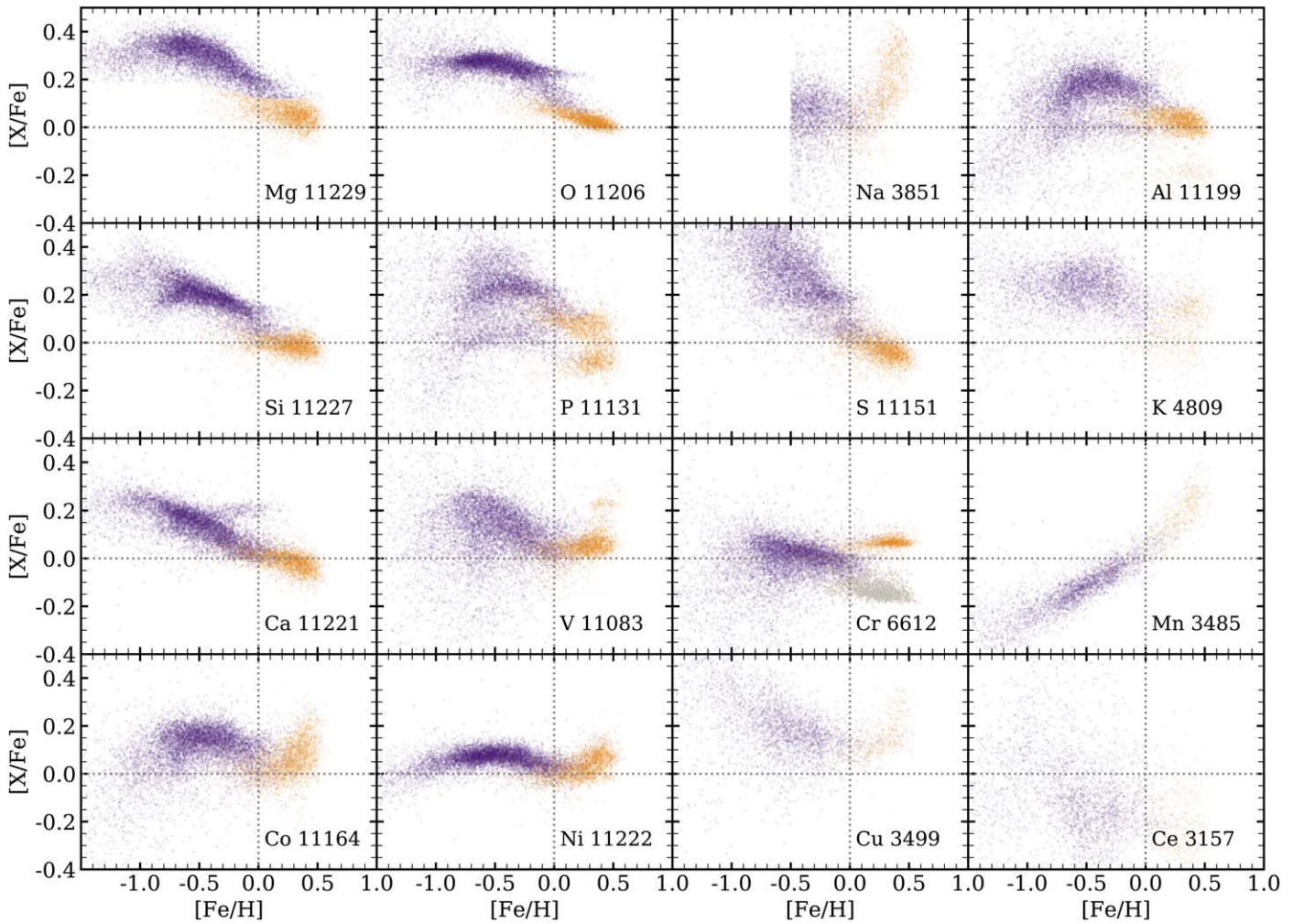


Figure 3. Bulge star distributions in $[X/Fe]$ vs. $[Mg/Fe]$ space for APOGEE elements. High-Ia stars are in orange, and low-Ia stars are in purple. The dotted lines in each panel denote solar $[X/Fe]$ and $[Fe/H]$. The number in the bottom right corner of each subplot corresponds to the number of stars for each elemental population that pass our cuts. Excluded Cr stars are in gray.

Section 1), as the bulge/disk division is not clearly defined. We investigate the radial dependence of the abundance trends in the inner Galaxy by subdividing the bulge ($R_{GC} < 3$ kpc) into three groups: $2 \text{ kpc} \leq R_{GC} < 3 \text{ kpc}$, $1 \text{ kpc} \leq R_{GC} < 2 \text{ kpc}$, and $R_{GC} < 1 \text{ kpc}$. For each group, we calculate the median high- and low-Ia trends and compare with the full sample. We find that the locations of the median trends are identical for all three groups within the uncertainties, though Mn, K, Cu, and Ce do not have enough stars on the high-Ia sequence to derive median trends for the innermost radial bin. We extend this comparison to the vertical bounds as well. Our bulge cut extends to high $|Z|$, so we divide the stars into two height bins of $|Z| < 0.25$ kpc and $1 \text{ kpc} \leq |Z| < 5 \text{ kpc}$ to probe the midplane and extended bulge. We again find that the high- and low-Ia trends remain constant. We do not see a radial or height dependence of the high- or low-Ia medians for stars within a radius of 3 kpc.

Our bulge definition is based on spatial location, and we do not attempt to distinguish between in situ and accreted populations, bulge and collocated halo stars, or heated disk stars and stars born in a spheroidal configuration. Definitions that include kinematic selection or use abundance to isolate accreted populations would lead to a different bulge sample. However, the similarity of median trends at low $|Z|$ and higher $|Z|$ and of the bulge and disk trends discussed below suggest that alternative bulge definitions

would not change our findings about median sequences, even though they might change the distribution of stars in $[Mg/H]$ and $[Fe/Mg]$. Das et al. (2020) and Horta et al. (2021) used the $[Mg/Mn]$ versus $[Al/Fe]$ diagram to identify stars with $-1.2 < [Fe/H] < -0.5$ that they suggest represent an accreted population. Figure 4 shows this diagram for the ~ 3400 stars of all metallicities in our sample that have the most reliable Mn abundances. We find ~ 450 stars in the region of parameter space that these papers describe as “the blob” and “the inner galaxy structure,” respectively. About 140 of these stars fall into the $-1.2 < [Fe/H] < -0.5$ metallicity range and thus may have been accreted. We refer to the above papers for further investigation of the kinematic and chemical origins of these stars.

Additionally, the Milky Way bar may have a distinct chemical signature. Work by Bovy et al. (2019) found that inner galaxy stars ($R_{GC} < 5$ kpc) inside and outside of the bar followed the same $[O/Fe]$ versus $[Fe/H]$ tracks, but that there were more metal-poor stars ($[Fe/H] < 0$) in the bar than the outside of the bar. Lian et al. (2021) found similarly small differences between the $[Fe/H]$ and $[Mg/Fe]$ distributions on and off the inner bar. We investigate whether the $[X/Mg]$ versus $[Mg/H]$ trends differ between on- and off-bar inner Galaxy regions. We use the bar definition from Bovy et al. (2019): an ellipse with a semimajor axis of 5 kpc angled at 25°

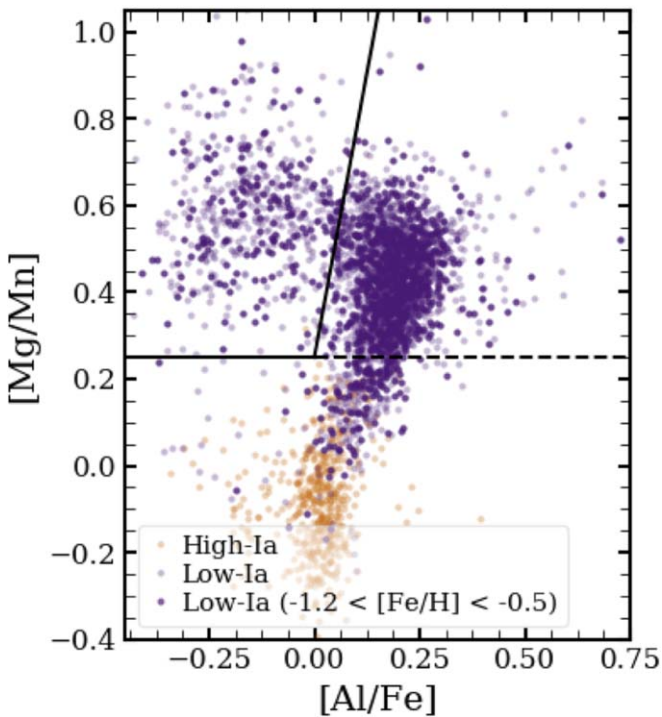


Figure 4. The $[Mg/Mn]$ vs. $[Al/Fe]$ distribution for ~ 3400 high-Ia (orange) and low-Ia (purple) stars. The solid and dashed lines are taken from Horta et al. (2021), where the solid lines separate stars with $-1.2 < [Fe/H] < -0.5$ of accreted origin (high $[Mg/Mn]$, low $[Al/Fe]$) from those of in situ formation, and the dashed line at $[Mg/Mn] = 0.25$ separates high and low- α stars. Our low-Ia stars with $-1.2 < [Fe/H] < -0.5$ are plotted in dark purple.

clockwise from the Sun–Galaxy line with an axis ratio of 0.4. We take the 2000 stars in this ellipse with $R_{GC} < 3$ kpc and find the median high- and low-Ia abundance trends for each element with sufficient observations. While the metallicity distribution varies, we find good agreement between the median tracks of the bar and the full inner galaxy population. Small differences (0.05 dex) are seen at the low- $[Mg/H]$ end of the low-Ia sequence for Al, Si, V, Cr, and Co. Many of these elements show the low abundance artifacts noted by J20, so the deviations are likely due to the small number of stars in the sample and the influence of these artifacts.

3.3. Creating a Comparison Sample

By comparing the median abundance trends of the bulge and disk, we can learn about the similarities and/or differences in their chemical enrichment histories. Upon first analysis of the bulge and W19 disk medians, we see differences of ~ 0.1 – 0.2 dex in half of the elements. The top row of Figure 5 shows those of Al and Si. The low-Ia $[Al/Mg]$ bulge sequence dips below that of the W19 disk at subsolar $[Mg/H]$. The differences in Si are subtler, but both the bulge high- and low-Ia medians appear suppressed relative to the disk.

These two populations, however, do not probe similar stellar samples. APOGEE observes different stellar samples at different locations in the Galaxy. As the bulge is farther away, APOGEE observes only the most luminous giants. This means that the $\log(g)$ distribution of stars differs between the bulge and the W19 disk (Figure 6, panels a and b). Systematic abundance errors that correlate with $\log(g)$ could cause artificial differences between the bulge and disk medians (e.g., Santos-Peral et al. 2020). To test this possibility, we randomly resample the full disk

population to reflect the $\log(g)$ distribution of the bulge. To ensure that we sample disk stars and not inner galaxy stars on the bulge border, we restrict our disk to $5 \text{ kpc} < R_{GC} < 11 \text{ kpc}$. In each $\log(g)$ bin, we select a number of APOGEE disk stars equal to the number of bulge stars in the same bin. We will hereafter refer to this stellar population as the “resampled disk.” Figure 6 plots histograms of the bulge and resampled disk’s $\log(g)$ distribution in panels a and c and their radial position in the bottom row (panel 4). Stars in both populations are distributed throughout the bulge and disk, respectively.

After this resampling, the median $[X/Mg]$ versus $[Mg/H]$ high- and low-Ia trends come into closer agreement for many elements. The middle row of Figure 5 compares $[Al/Mg]$ and $[Si/Mg]$ versus $[Mg/H]$ medians for the bulge and the $\log(g)$ resampled disk. Differences seen between the W19 disk and bulge almost disappear. To confirm that this is a result of $\log(g)$ systematics and dissimilar sampling, we repeat for the opposite case, randomly resampling the bulge to reflect the $\log(g)$ distribution of the W19 disk. We again see that the median $[Al/Mg]$ and $[Si/Mg]$ versus $[Mg/H]$ trends agree between the two populations with similar $\log(g)$ distributions (Figure 5, bottom row). We conclude that $\log(g)$ systematics cause small but detectable changes in the elemental median trends. In order to accurately compare Galactic regions, we must have samples with similar $\log(g)$ distributions. Our bulge and resampled disk populations satisfy this requirement.

This resampling also removes the bias from NLTE corrections. Jönsson et al. (2020) noted that elements such as Mg, Al, K, and Ca might be influenced by NLTE effects not accounted for in APOGEE’s current data reduction pipeline. These effects may be responsible for shifts in abundances between dwarf and giant stars. Our $\log(g)$ constraints ensure that our bulge and disk populations have the same stellar makeup, so a relative abundance comparison should see no influence from NLTE effects.

A density plot of our resampled disk can be found in Figure 7. We use the same low-Ia definition as in Equation (1). The high- and low-Ia populations are clearly defined and separated. The resampled disk has more stars on the high-Ia sequence and a less extended low-Ia sequence than the bulge, reflective of the distribution found by W19. We apply the same exclusions to the resampled disk as described above.

3.4. Comparison to APOGEE Disk

Now that we have similar stellar samples, we can compare the high- and low-Ia median abundance trends of the bulge and resampled disk. Figure 8 plots the median bulge trends (same as Figure 2) and the median trends of the resampled disk. Both are binned by 0.1 dex in $[Mg/H]$, requiring >20 stars per bin. Overall, the medians agree well. The resampled disk and bulge trends are nearly identical for Fe, O, Al, Si, S, K, Ca, V, Cr, Ni, and Cu. This similarity suggests that the bulge and disk experienced similar chemical enrichment and that nucleosynthesis pathways are identical throughout the Galaxy, extending the conclusions of W19 from the disk to the inner Galaxy. We do see minor differences between the Na, P, Mn, Co, and Ce trends of the bulge and resampled disk. All of these differences, though, are on the scale of 0.1 dex or smaller (see Figure 13). In the following subsections, we will more closely examine the median trends, discussing APOGEE’s elemental precision, nucleosynthetic origins, and differences/similarities between the bulge and the resampled disk. We will reference the

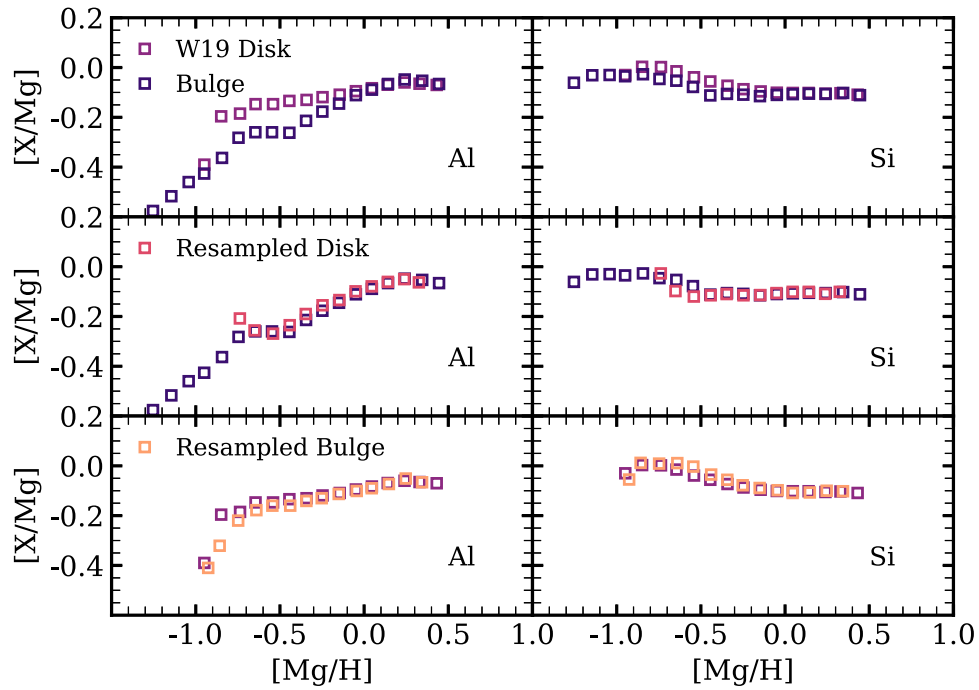


Figure 5. Median low-Ia trends for Al and Si, comparing different stellar samples. Top row: bulge medians (dark purple) compared to W19 disk medians (light purple). Middle row: bulge medians (purple) compared to disk stars of $5 \leq R_G \leq 11$ whose $\log(g)$ distribution matches that of the bulge (resampled disk; pink). Bottom row: W19 disk medians (pink) compared to a subset of stars in the bulge sample that reproduce the $1 < \log(g) < 2$ distribution of the W19 disk (resampled bulge; orange). After $\log(g)$ systematics are accounted for in the lower two rows, the differences seen in the top row disappear.

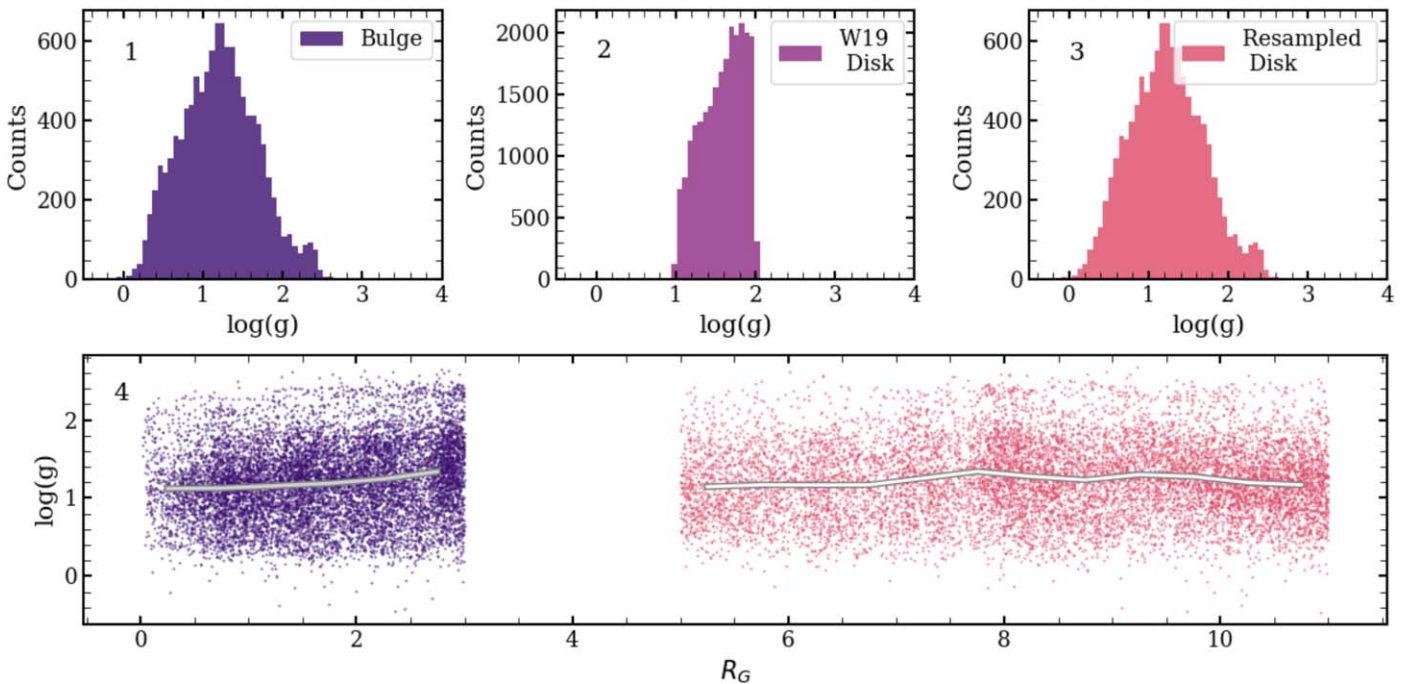


Figure 6. Top row: $\log(g)$ distributions for stars in the bulge (left; dark purple), W19 disk sample (middle; purple), and resampled disk (right; pink). Bottom: radial location of stars with a given $\log(g)$ for the bulge and resampled disk populations. We overplot median trends binned radially by 0.5 kpc. Bulge and disk stars appear evenly radially distributed with no clear dependence on $\log(g)$.

chemical evolution models of Andrews et al. (2017, hereafter AWSJ17), for theoretical yield predictions.

3.4.1. α -elements

The CCSNe dominate the production of α -elements such as O, Si, S, and Ca. O is predicted to come almost entirely from

CCSNe, as is Mg, while Si, S, and Ca have some SN Ia contribution (AWSJ17). As such, we see that O traces Mg and has little to no separation between the high- and low-Ia $[O/Mg]$ medians. APOGEE's $[O/Mg]$ trends are flat, supporting metallicity-independent CCSN yields. This agrees with other IR studies (J20) but is inconsistent with metallicity-dependent $[O/Mg]$ trends derived from optical abundances (GJW).

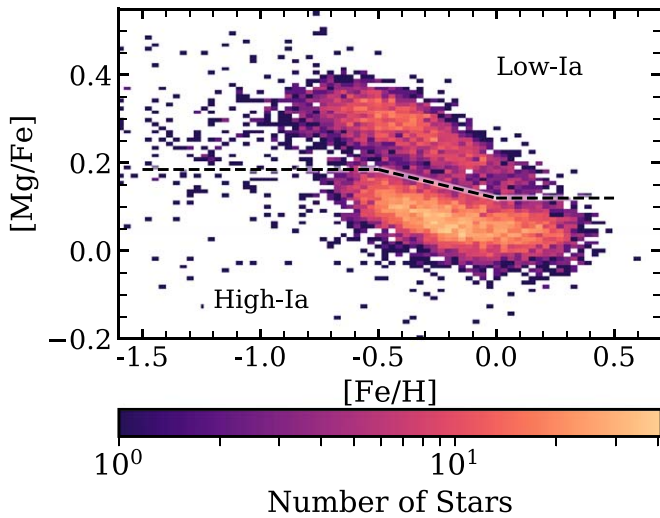


Figure 7. Density plot of the stars in the resampled disk that recreate the $\log(g)$ distribution of the bulge. The dashed line denotes our division between the high- and low-Ia stars used in the bulge. The two sequences can be clearly distinguished, as in Figure 1 of W19.

Here Si and Ca show larger median high- and low-Ia separations than O, in agreement with theoretical predictions that they have a nondominant SN Ia contribution. We note that Si is one of the most precisely measured elements in APOGEE with a scatter of $\lesssim 0.02$ dex (J20). While AWSJ17 found that S has a larger SN Ia contribution than Si, we see no separation between the S high- and low-Ia median trends, indicative of little SN Ia contribution. Sulfur is the only α -element for which we infer metallicity-dependent yields.

The high- and low-Ia median trends of the α -elements agree very well between the bulge and the resampled disk. The median absolute differences between the sequences are all ≤ 0.02 dex and within observational errors. We do not see the enhancement in the bulge α abundances relative to the local thick disk at a given metallicity, as was found in previous works (e.g., Bensby et al. 2013; Johnson et al. 2014).

3.4.2. Light Odd-Z Elements

Like the α -elements, we expect CCSNe to be the predominant source of the light odd-Z elements (Na, Al, P, and K) and SNe Ia to contribute in a nondominant way. The abundance tracks of these elements, however, should be distinguished from α -elements by stronger metallicity dependence (AWSJ17). While $[\text{Na}/\text{Mg}]$ high- and low-Ia median trends do show a positive metallicity gradient, they also show a significant separation. This suggests a large SNe Ia or other delayed production source. The median trend separation agrees with results for the APOGEE DR14 disk (W19) and GALAH DR2 sample (GJW). Both papers include a larger discussion of the nucleosynthetic implications of the empirical results. We see a relatively similar sequence separation in the Na trends of the resampled disk and bulge, but the two samples have different high-Ia metallicity dependencies. While the low-Ia tracks are in good agreement, the high-Ia trends have a median absolute difference of 0.06 dex, one of the largest differences between the bulge and the resampled disk. We reiterate that Na is not precisely determined by APOGEE (with a scatter of ~ 0.1 dex), and that temperature systematics have not been accounted for (J20). The difference between bulge and disk trends for the high-Ia population could be a result of different

chemical enrichment histories, but it could also be a result of residual systematic errors on Na abundance measurements.

The Al and P are also plagued by systematics and reduction artifacts. Both show some separation in their median trends, though not to the extent of Na. This separation is unexpected for Al, which is predicted to be a pure CCSN element (AWSJ17). No separation in their analysis of DR14 data was found by W19. The Al trends do show a positive metallicity dependence, as expected. The bulge and resampled disk $[\text{Al}/\text{Mg}]$ trends agree well after the disk resampling. The Al abundances have high precision ($\lesssim 0.04$ dex) in APOGEE DR16 (J20).

The $[\text{P}/\text{Mg}]$ trends show 0.05–0.1 dex differences between the bulge and the resampled disk in some $[\text{Mg}/\text{H}]$ bins. A closer examination of stars in the high-Ia and low- $[\text{Mg}/\text{H}]$ bins—most discrepant between the bulge and the disk—reveals that the $\log(g)$ distribution of stars in the respective populations differs significantly. While the resampled disk stars span the parent sample’s $\log(g)$ range of 0–2.5, the less populated bulge bin only includes stars near $\log(g) = 0$, perhaps because only the most luminous stars yield successful P measurements at low $[\text{Mg}/\text{H}]$ at these distances. The $\log(g)$ systematics could be responsible for some of the median bin differences. We reiterate that P is the least precisely determined element in APOGEE (with scatter of 0.15 dex or greater) and subject to systematic errors (J20). Masseron et al. (2020), for example, found that low-metallicity P-rich stars are missed by ASPCAP entirely. We do not trust the P abundances and do not draw conclusions from these median trends.

We see the weakest metallicity dependence of the light odd-Z elements in the $[\text{K}/\text{Mg}]$ median trends. The high- and low-Ia medians show little separation and suggest CCSN-dominated production. This agrees with theoretical yields (AWSJ17). We see good agreement between the bulge and the resampled disk, though the resampled disk’s low-Ia median trend sits at a higher $[\text{K}/\text{Mg}]$ than the bulge’s low-Ia median.

3.4.3. Fe-peak Elements

Nucleosynthetic yields and chemical evolution models predict comparable CCSN and SN Ia contribution to Fe-peak elements at solar abundances (AWSJ17). Our observations agree, as we see significant separation between the high- and low-Ia median trends for all APOGEE Fe-peak elements. Further, AWSJ17 predicted that the odd-Z elements (V, Mn, and Co) will have a positive metallicity dependence, while the even-Z elements (Cr, Fe, and Ni) will have flatter trends. We observe Mn and Co to have a stronger metallicity dependence than the even-Z elements. Here V exhibits a shallower trend than Co and Mn; $[\text{V}/\text{Mg}]$ and $[\text{Co}/\text{Mg}]$ have a similar small separation between the high- and low-Ia median trends, indicative of significant but nondominant SN Ia contribution. As in W19 and GJW, Mn has the largest separation of all included elements and thus the largest SN Ia contribution. Among the even-Z elements, $[\text{Cr}/\text{Mg}]$ trends show larger separation than $[\text{Fe}/\text{Mg}]$ (with the caveat that we cut out low- $[\text{Cr}/\text{Mg}]$, high-Ia stars as discussed in Section 3.1), while $[\text{Ni}/\text{Mg}]$ trends show less separation. This suggests that SNe Ia dominate Cr production, while CCSNe make a larger contribution to Ni. Both elements strongly resemble Fe.

The V, Cr, Fe, and Ni median trends agree well between the bulge and resampled disk. All have absolute median differences ≤ 0.02 dex. Both populations’ $[\text{Fe}/\text{Mg}]$ low-Ia median sequences plateau around -0.3 . The Mn and Co show larger differences. Both the high- and low-Ia resampled disk $[\text{Mn}/\text{Mg}]$ median

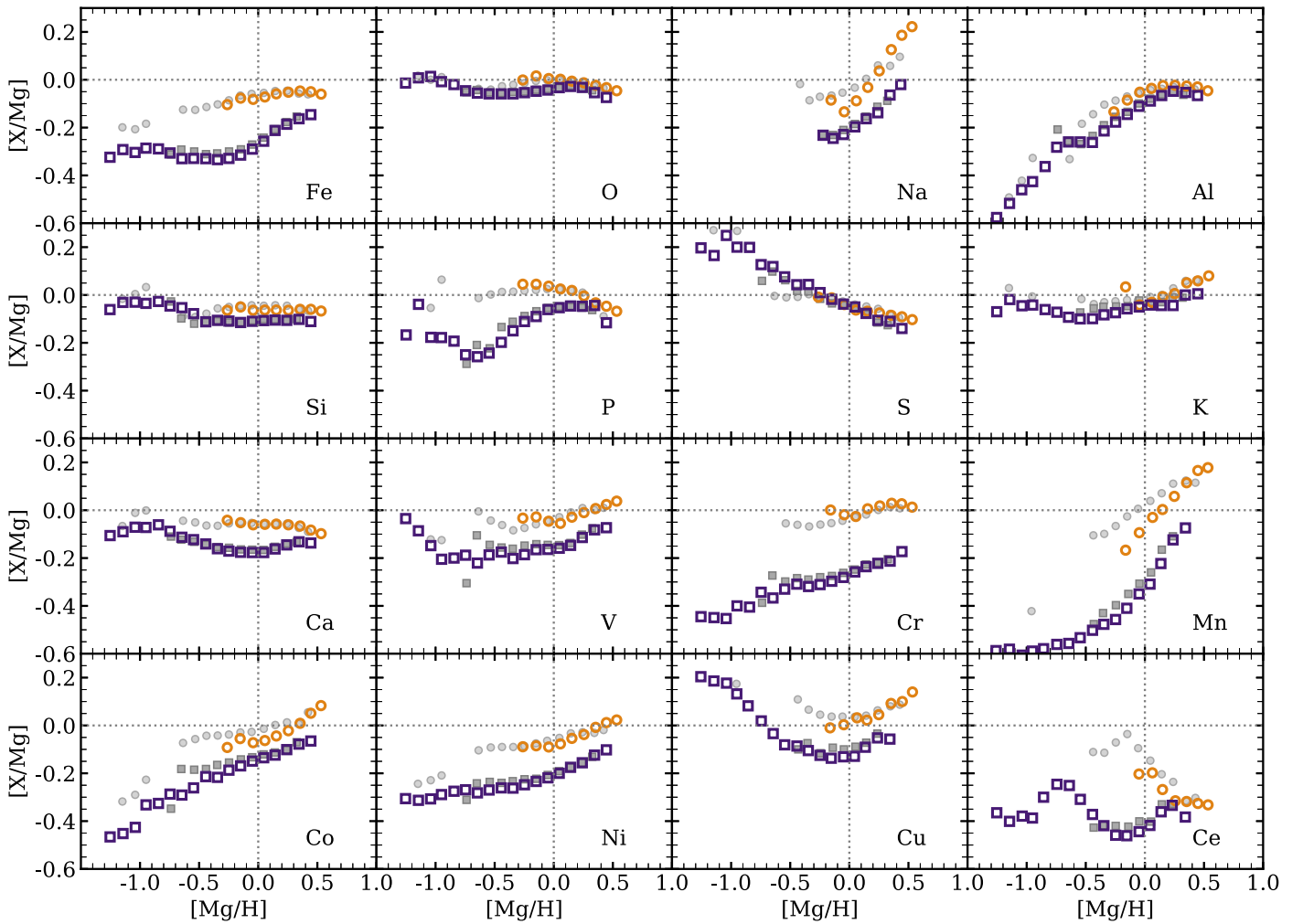


Figure 8. APOGEE bulge star median abundances trends of high-Ia (orange circles) and low-Ia (purple squares) populations, as in Figure 2. Median high- and low-Ia abundances of resampled disk stars are plotted as light gray circles and dark gray squares, respectively, for comparison. Dotted lines correspond to solar values of $[X/Mg]$ and $[Mg/H]$.

trends sit at slightly higher $[Mn/Mg]$ than those of the bulge and have a flatter metallicity dependence. The bulge and resampled disk’s high- and low-Ia $[Mn/Mg]$ trends have median absolute differences of 0.07 and 0.05 dex, respectively. We reiterate that APOGEE DR16 Mn abundances are not populated for cool stars ($T \lesssim 4000$ K) due to temperature systematics, so we have a much smaller sample than the rest of the bulge with few high-Ia stars. While cluster calibrations were applied to DR14 data to remove temperature effects (Holtzman et al. 2018), these calibrations were not done in DR16. The Mn shows some of the largest differences between the bulge and the resampled disk, particularly for high-Ia stars, but due to the small bulge sample and potential temperature systematics, we interpret these results cautiously. The Co high- and low-Ia resampled disk medians are slightly higher in $[Co/Mg]$, with flatter metallicity dependence than the bulge. The deviations in the Co low-Ia trends seen at subsolar $[Mg/H]$ can also be seen, to a much smaller degree, in Ni and V.

3.4.4. Cu and Ce

In GJW, we classify Cu as an “Fe-cliff” element, as it resides on the steeply falling edge of the Fe abundance peak. APOGEE DR16+ Cu abundances are not the most reliable, having a low

precision and low accuracy (J20). The upturned tail at low $[Mg/H]$ and $[Fe/H]$ seen in Figures 2 and 3 is unexpected and probably not trustworthy. We will limit our interpretation to Cu abundances above solar $[Mg/H]$. Here we see a separation between the high- and low-Ia sequences and a positive metallicity dependence. Production of Cu is thought to be dominated by CCSNe, with yields suggesting a strong metallicity dependence (W19). The observed separation in median trends, however, implies a nonzero SN Ia or other delayed component, in agreement with optical trends from GALAH (GJW). At all metallicities, we see a good agreement between the bulge and resampled disk median trends.

While all of the above elements are likely produced through CCSN and SN Ia nucleosynthesis, Ce is produced by a combination of the rapid and slow neutron-capture processes (r - and s -process, respectively).¹⁷ Separation in the Ce high- and low-Ia median trends indicates that Ce is dominated by a delayed enrichment source, in agreement with measurements by Arlandini et al. (1999) and Bisterzo et al. (2014), who found

¹⁷ The r - and s -processes do not automatically translate into prompt and delayed, since, for example, some s -process production occurs in massive CCSN progenitors. In practice, most s -process enrichment arises in AGB stars with intermediate lifetimes, and the main sources of r -process enrichment appear to be prompt.

Ce to have $\sim 80\%$ *s*-process contribution. We see a similar sequence separation between the bulge and the resampled disk, though the resampled disk’s low-Ia trend has slightly higher [Ce/Mg] than that of the bulge. This difference should be viewed with some caution, as APOGEE Ce abundances have low precision (scatter of 0.15 dex or greater) due to their single line analysis (J20). We do, however, think that Ce abundances are accurate (excluding low-metallicity stars). Neutron-capture elements are not well studied in the bulge, so APOGEE Ce observations can give insight into nucleosynthetic processes beyond CCSNe and SNe Ia.

The DR16 data set is the first APOGEE data release to include Cu and Ce. A larger discussion of their abundance trends, nucleosynthetic implications, and comparison to GALAH data can be found in Appendix B.

4. Two-process Model

With the exception of Ce, the elements studied in this paper are theoretically expected to originate almost entirely from CCSNe or SNe Ia (Johnson 2019). While individual CCSNe produce elements in different ratios depending on progenitor mass, the IMF-averaged production should yield fixed ratios for SNe of a given metallicity. The median abundance ratio sequences from APOGEE DR14 were interpreted by W19 in terms of a two-process model, which represents the elemental abundances of any given star (or median sequence point) as the sum of a CCSN process with amplitude A_{cc} and an SN Ia process with amplitude A_{Ia} :

$$\left(\frac{X}{H}\right) = A_{cc}p_{cc}^X(Z) + A_{Ia}p_{Ia}^X(Z). \quad (2)$$

To account for metallicity-dependent yields, the process vectors p_{cc}^X and p_{Ia}^X are allowed to depend on the star’s metallicity. The analysis was extended to GALAH DR2 abundance ratios by GJW, including elements not measured by APOGEE. In W19, GJW, and this paper, the metallicity dependencies are modeled as power laws in (Mg/H), with index α_{cc} and α_{Ia} for p_{cc}^X and p_{Ia}^X , respectively.

Here we fit the DR16 abundance ratio sequences of the resampled disk to infer the two-process model parameters α_{cc} , α_{Ia} , and

$$R_{Ia}^X = \frac{p_{Ia,\odot}^X}{p_{cc,\odot}^X}, \quad (3)$$

which is the ratio of the two processes for element X in a star with solar abundances [Mg/H] = [Fe/Mg] = 0. Differences from W19 arise partly from the differences between DR14 and DR16 abundance determinations and partly from the different log(*g*) distributions of the samples. The values of R_{Ia}^X , α_{cc} , and α_{Ia} derived here are not necessarily more reliable than those of W19, but they allow us to predict bulge star abundances using a model “trained” independently on the disk. In Section 5, we use these comparisons to place rough limits on the possible difference between the high-mass IMF slope of bulge and disk populations.

As in W19, we assume that Mg is purely produced by CCSNe with metallicity-independent yields ($R_{Ia}^{Mg} = 0$ and $\alpha_{cc}^{Mg} = \alpha_{Ia}^{Mg} = 0$), Fe is produced by both SNe Ia and CCSNe with metallicity-independent yields ($\alpha_{cc}^{Fe} = \alpha_{Ia}^{Fe} = 0$), and stars

on the low-Ia plateau, at [Mg/Fe] ≈ 0.3 , have pure CCSN enrichment (implying $R_{Ia}^{Fe} = 1$). Therefore, given any star’s [Mg/Fe], the ratio of its SNe Ia to CCSN enrichment is

$$\frac{A_{Ia}}{A_{cc}} = 10^{0.3 - [Mg/Fe]} - 1. \quad (4)$$

From the global elemental parameters (R_{Ia}^X , α_{cc} , and α_{Ia}) and stellar abundances ([Mg/H] and [Mg/Fe]), W19 derived an expression to calculate the expected abundance of element X in a star as

$$[X/Mg] = \alpha_{cc}[Mg/H] + \log \left[\frac{1 + R_{Ia}^X(A_{Ia}/A_{cc})10^{(\alpha_{Ia} - \alpha_{cc})[Mg/H]}}{1 + R_{Ia}^X} \right], \quad (5)$$

with A_{Ia}/A_{cc} from Equation (4). As in W19 and GJW, we will use the median [X/Mg] and [Mg/H] trends to find the best R_{Ia}^X , α_{cc} , and α_{Ia} values for each element. For elements that have substantial production by asymptotic giant branch (AGB) stars (Ce and possibly Na, P, and Cu), the model parameters are only qualitatively meaningful, since the AGB enrichment delay is different from that of SNe Ia.

4.1. Fitting the Resampled Disk

We perform an unweighted least-squares fit to the resampled disk’s high- and low-Ia [Mg/H] versus [X/Mg] median trends for each element with the two-process model to derive the best-fit R_{Ia}^X , α_{cc} , and α_{Ia} values. We allow all three parameters to vary and conduct a grid search with a step size of 0.01 for each. Due to the low number of stars at low metallicity, we only fit median points with [Mg/H] > -0.7 . We choose to fit the resampled disk rather than the bulge because the resampled disk medians track the bulge medians and its high-Ia sequence is better populated.

As pointed out by GJW (see their Figure 10), the two-process model necessarily predicts [X/Mg] = 0 for a star, or median sequence point, with [Fe/Mg] = [Mg/H] = 0. Figure 8 shows that this is not the case for all elements in our sample, but the small departures from solar [X/Mg] on the high-Ia sequence are plausibly a consequence of small calibration errors in the abundance determinations. Following GJW, therefore, we apply zero-point offsets to all elements in order to force the high-Ia sequence to pass through [X/Mg] = 0 at [Mg/H] = 0 prior to performing the fits. These offsets are listed in Table 3 and applied to the bulge and resampled disk sequences in all further analysis. We note that APOGEE does already apply zero-point offsets to force stars with solar [M/H] in the solar neighborhood to have a mean [X/M] = 0 (J20), but the log(*g*) distribution of that sample is different from ours. (See GJW’s Figure 10 for an example of two-process fits with and without zero-point offsets.)

Under the two-process model, elements solely produced by CCSNe should have no separation between their high- and low-Ia median sequences and be best fit by $R_{Ia}^X \approx 0$. As the SN Ia contribution to an element increases, the sequence separation should also increase, driving the R_{Ia}^X value up. Elements with $R_{Ia}^X \approx 1$ are produced equally by CCSNe and SNe Ia in stars of solar abundance, and SNe Ia dominate the production of those with $R_{Ia}^X > 1$. The R_{Ia}^X value can be converted to a CCSN

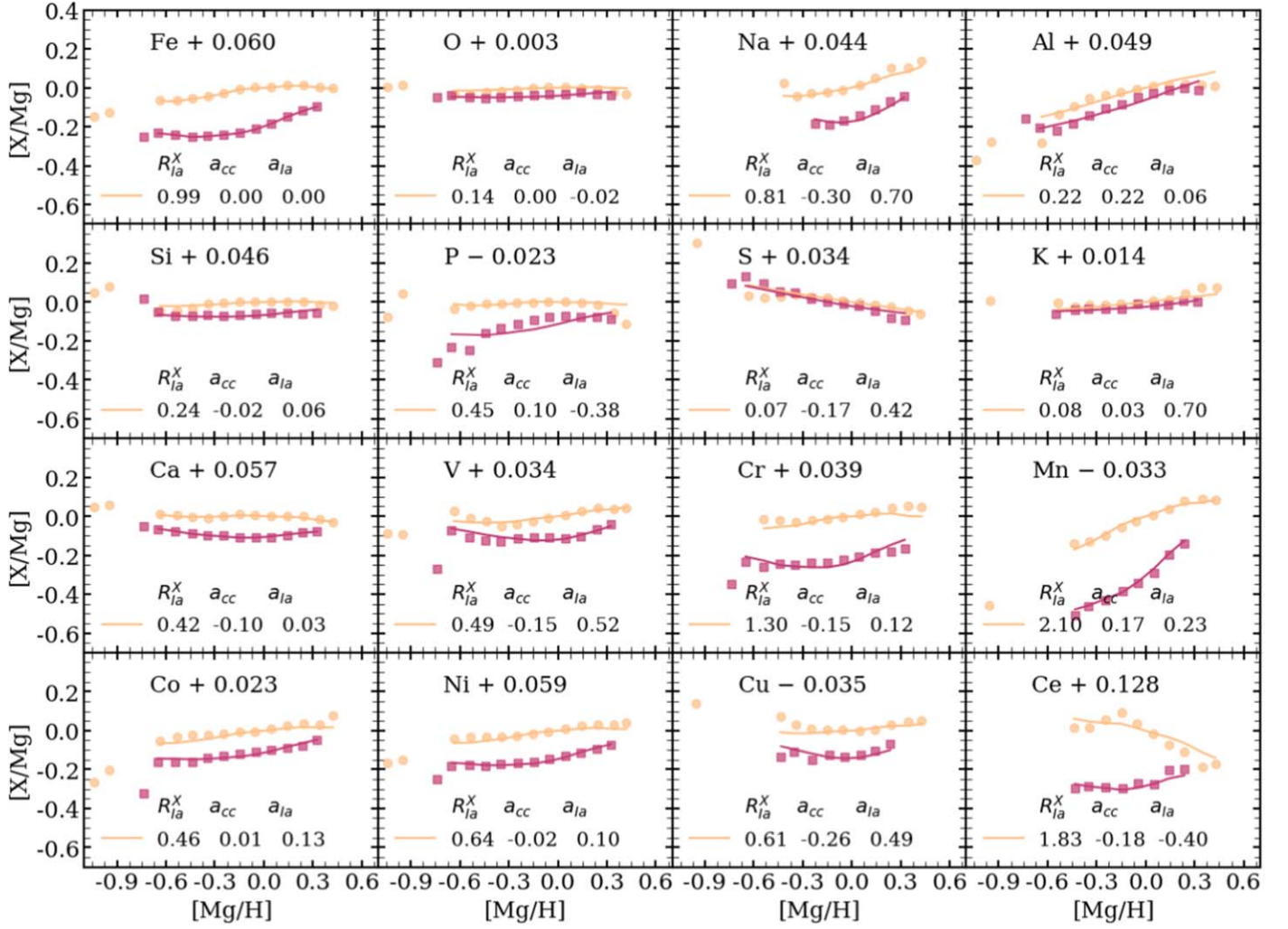


Figure 9. Two-process model fits to the resampled disk median trends. Orange/pink circles/squares represent the high-/low-Ia population medians including offsets. Solid lines are the best-fit two-process sequences. Best-fit sequences only extend to a lower bound of $[\text{Mg}/\text{H}] = -0.7$, as fits were computed on median points with $[\text{Mg}/\text{H}] \geq -0.7$. Elemental best-fit two-process values and zero-point offsets are given in each cell.

fraction by the equation

$$f_{cc} = \frac{1}{(1 + R_{Ia}^X)}. \quad (6)$$

Elements with $\alpha_{cc} \approx \alpha_{Ia} \approx 0$ and $R_{Ia}^X \approx 1$ will have median $[\text{X}/\text{Mg}]$ trends that follow the corresponding $[\text{Fe}/\text{Mg}]$ sequences. As α_{cc} increases, the slope of both sequences should also increase, with positive/negative α_{cc} representing a positive/negative metallicity dependence. The α_{Ia} parameter will further change the slope of the high-Ia sequence relative to the low-Ia sequence.

Figure 9 shows the two-process model fits to the resampled disk's high- and low-Ia medians (including an offset). The R_{Ia}^X , α_{cc} , and α_{Ia} values for each element, as well as the zero-point offset applied prior to the fit, are listed in the respective panels and Table 3. The two-process model well describes the high- and low-Ia trends of the resampled disk down to $[\text{Mg}/\text{H}] = -0.7$ for most elements. However, we see that the Al, P, and Cr high-Ia medians are poorly fit at the high- $[\text{Mg}/\text{H}]$ end and that the two-process model is unable to reproduce the nonlinear metallicity dependence of the $[\text{Cu}/\text{Mg}]$ and $[\text{Ce}/\text{Mg}]$

Table 3

Zero-point Offsets and the Best-fit Two-process Model Parameters for Each Element as Fit to the Median High- and Low-Ia Points of the Resampled Disk

$[\text{X}/\text{Mg}]$	Offset	R_{Ia}^X	α_{cc}	α_{Ia}	f_{cc}
Fe	0.060	0.99	0.00	0.00	0.503
O	0.003	0.14	0.00	-0.02	0.877
Na	0.044	0.81	-0.30	0.70	0.552
Al	0.049	0.22	0.22	0.06	0.820
Si	0.046	0.24	-0.02	0.06	0.806
P	-0.023	0.45	0.10	-0.38	0.690
S	0.034	0.07	-0.17	0.42	0.935
K	0.014	0.08	0.03	0.70	0.926
Ca	0.057	0.42	-0.10	0.03	0.704
V	0.034	0.49	-0.15	0.52	0.671
Cr	0.039	1.30	-0.15	0.12	0.435
Mn	-0.033	2.10	0.17	0.23	0.323
Co	0.023	0.46	0.01	0.13	0.685
Ni	0.059	0.64	-0.02	0.10	0.610
Cu	-0.035	0.61	-0.26	0.49	0.621
Ce	0.128	1.83	-0.18	-0.40	0.353

Note. Here f_{cc} denotes the fractional CCSN contribution, as defined in Equation (6).

trends. If we allowed arbitrary metallicity dependencies, then the two-process model would be able to fit the observed median sequences by construction, so imperfect fits are a consequence of the power-law restriction. Comparisons like Figure 9 are not in themselves a strong test of the two-process model’s underlying assumptions; rather, these fits allow us to convert the observed sequences into physically meaningful quantities given those assumptions. Better tests of the model’s validity come from predicting the abundance trends of other stellar populations or star-by-star deviations from median trends, which we will examine briefly in Section 4.2 and in more detail in future work.

Two-process fits to the APOGEE DR14 disk for all elements included here except Cu and Ce (new to DR16) were reported by W19. They discussed each element, its two-process model fit, and the nucleosynthetic implications, and they compared the derived f_{cc} value to theoretical results from Rybizki et al. (2017). We find very similar f_{cc} values (a difference of $\leq 10\%$) for Fe (by construction) and for O, Na, Si, S, Ca, Cr, Mn, and Ni, so we do not go into detail about the two-process model implications in this paper. We discuss the two-process model implications for Cu and Ce in Appendix B.

We do, however, see differences between our derived two-process fits and those of W19 for Al, P, K, V, and Co. In all of these cases, we have repeated our fits using the DR16 abundances but the disk $\log(g)$ and geometry cuts used by W19. The differences persist, indicating that they arise primarily from changes in the ASPCAP abundance pipeline, not from differences in the $\log(g)$ distribution or location of the sample. For Al, the higher $f_{cc} = 0.97$ found by W19 (versus 0.82 here) is in better agreement with theoretical expectations that Al is an almost pure CCSN element. Conversely, for K, the higher $f_{cc} = 0.94$ (versus 0.80 in W19) agrees better with the expectation that CCSNe dominate its production. For Co, we find $f_{cc} = 0.69$ versus $f_{cc} = 0.80$ in W19, in better agreement with the GJW findings from GALAH but lower than predicted by the yield models of Rybizki et al. (2017). For P and V, a smaller separation of $[X/Mg]$ values in DR16 leads to higher inferred values of f_{cc} . It was stressed by J20 that P and V are two of the least precise and potentially least accurate abundances in DR16. We do not have simple explanations for these differences or a clear indication of which abundances are more accurate for a given element, DR14 or DR16. The enormous sample size and generally high abundance precision in APOGEE allow us to see artifacts that would be hidden in smaller samples or less precise data. The artifacts discussed in Section 3.1 and the two-process parameter differences discussed here imply that systematic uncertainties remain in the APOGEE measurements at a level that is physically interesting.

4.2. Predicting Bulge Abundances

Using Equations (4) and (5), as well as the best-fit two-process model parameters from Table 3, we can predict the full set of abundance ratios for any star given only its $[Mg/H]$ and $[Fe/Mg]$ values. If the disk and bulge are enriched by the same nucleosynthetic processes, then the two-process model parameters used to describe the disk should accurately predict the bulge abundances. To test this, we calculate the APOGEE abundance suite of every bulge star using the model parameters from the resampled disk. These predicted distributions in $[X/Mg]$ versus $[Mg/H]$ space are shown in Figure 10. Median

trends of the high- and low-Ia bulge populations (Figure 2) are overplotted for comparison, including the zero-point offsets discussed above. As we only fit the two-process model above $[Mg/H] = -0.7$, trends below this metallicity are not included in our subsequent comparison and analysis but are included in the plot for completeness.

The $[Fe/Mg]$ versus $[Mg/H]$ predicted abundances are identical to those observed, by construction. All elements with low R_{Ia}^X values have “tight” predicted abundance distributions and little spread. This is a direct result of the two-process model assumptions; elements whose production is dominated by CCSNe should trace Mg and have little to no separation between the high- and low-Ia sequences. We do not add spread induced by observational errors to our predictions, so the width of our predicted abundance distributions is smaller than that of the observed distributions (Figure 2). The only source of scatter in the two-process predictions comes from the scatter of $[Fe/Mg]$ at fixed $[Mg/H]$, which is interpreted as star-to-star variations in the SN Ia-to-CCSN enrichment ratio A_{Ia}/A_{cc} . For elements with $R_{Ia}^X \approx 0$ ($f_{cc} \approx 1$), the induced scatter is minimal because SNe Ia do not contribute to this element in any case.

Figure 10 shows good agreement between the predicted abundances and observed bulge median trends of most elements. The most noticeable exceptions are for Na, Al, P, and Ce, particularly at supersolar metallicities. For Na, this difference reflects the difference in the observed median sequences of the resampled disk and bulge (Figure 8). For Al, P, and Ce, the power-law form of the two-process model leads to overpredicting the disk trends themselves at high $[Mg/H]$ (Figure 9), leading to overprediction of the bulge trends. The trends for many elements diverge from predictions below $[Mg/H] = -0.7$ because the power-law extrapolation of the two-process model becomes inaccurate.

Interestingly, for $[Mn/Mg]$, the agreement between predicted and observed trends in Figure 10 is better than the agreement of the observed medians in Figure 8. This improvement arises at least partly because the median $[Fe/Mg]$ values are slightly lower for the bulge than for the resampled disk. Within the two-process model, this difference implies that bulge stars have slightly lower SN Ia contributions at a given $[Mg/H]$. Because Mn has a large inferred $R_{Ia}^X = 2.1$, this difference translates into lower predicted $[Mn/Mg]$ for the bulge, producing better agreement. Given the observational uncertainties, these improvements could be a fluke, but they could be a sign that the two-process description is correctly capturing the impact of subtle differences in the relative SN Ia/CCSN contributions between the disk and the bulge.

To better quantify the similarities and differences between the observed and predicted populations, we calculate the median of the absolute differences,

$$\text{median}(|[X/Mg]_{\text{obs}} - [X/Mg]_{\text{pred}}|), \quad (7)$$

for each element, including the corrective offsets. In principle, the two-process model should be a better predictor of the elemental abundances than the median value of stars on the same sequence with the same $[Mg/H]$ because the model accounts for star-by-star scatter in A_{Ia}/A_{cc} . To test this expectation, we compare the median absolute difference of the observed and predicted abundances to the median absolute difference of the observed abundance and the median $[X/Mg]$

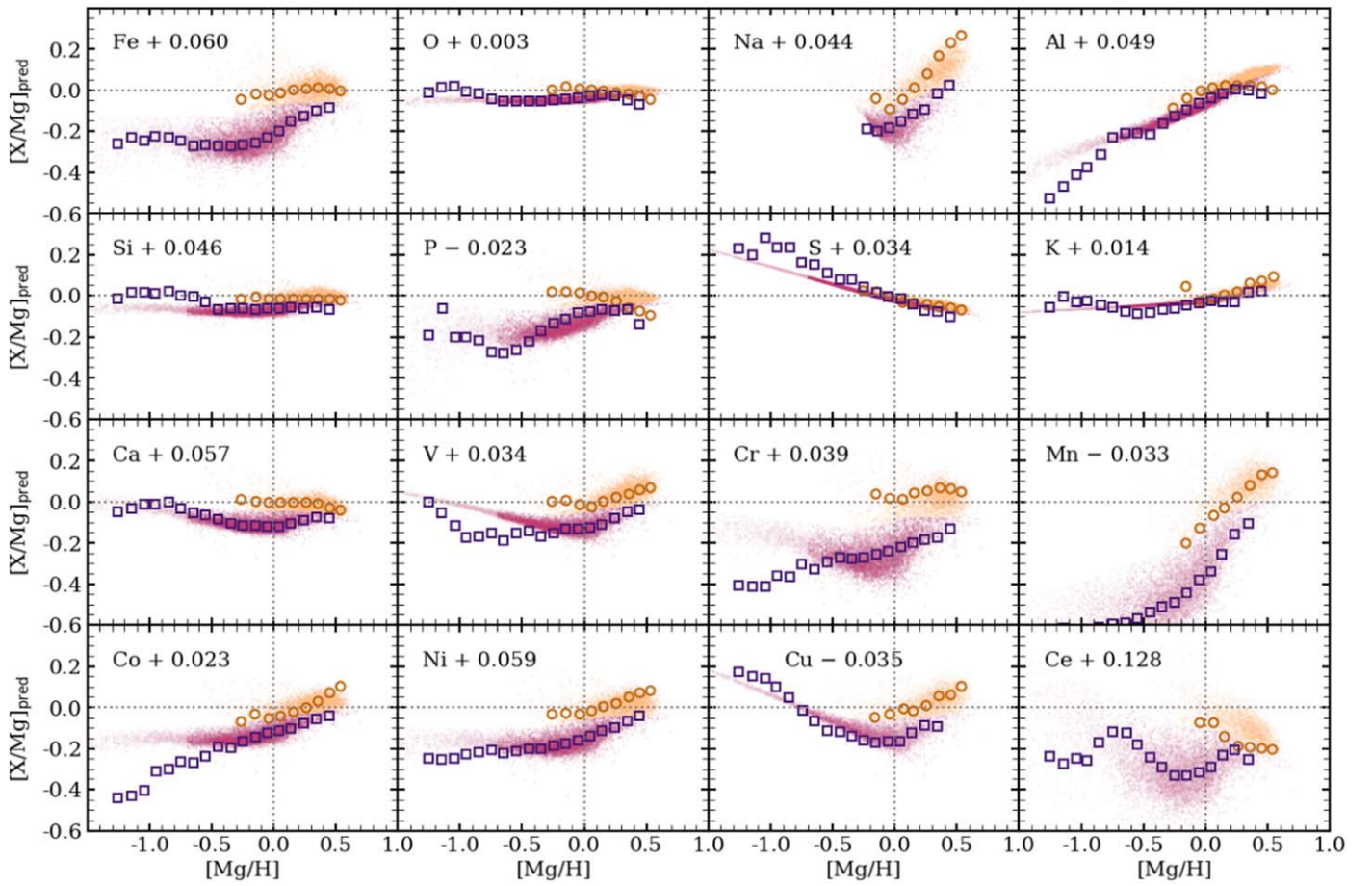


Figure 10. Predicted abundances for the bulge population given the resampled disk’s two-process model parameters. For each bulge star, $[X/Mg]$ values are predicted based on the star’s measured $[Mg/H]$ and $[Fe/Mg]$. Low-/high-Ia stars are colored pink/orange, respectively. Lighter shades indicate extrapolated abundance predictions ($[Mg/H] < -0.7$). The bulge median observed high- and low-Ia trends, including offsets listed in the top left corner, are overplotted in dark orange circles and purple squares, respectively.

value for a given $[Mg/H]$ bin,

$$\text{median}(|[X/Mg]_{\text{obs}} - [X/Mg]_{\text{med}}|). \quad (8)$$

We plot both statistics for the high-Ia (top) and low-Ia (bottom) populations of all elements in Figure 11. We only consider stars with $[Mg/H] > -0.7$, as the two-process model was only fit for such stars.

To first approximation, Figure 10 shows similar median absolute difference statistics for all elements, regardless of whether the two-process model or the observed median sequence is used to predict a star’s $[X/Mg]$. This similarity suggests that most of the scatter in $[X/Mg]$ arises from observational errors, and the median absolute differences are indeed largest for elements measured with relatively low precision, such as Na, P, and K. For the high-Ia population, the two-process model predicts $[Al/Mg]$ and $[Ca/Mg]$ worse than the corresponding median trend because it also predicts the median trend itself poorly (see Figure 10). For the low-Ia population, the two-process prediction is more accurate than the observed median trend for Fe-peak elements, particularly for $[Mn/Mg]$ and $[Ni/Mg]$. This admittedly subtle difference indicates that star-by-star deviations for Fe-peak elements track the SN Ia contribution to $[Fe/Mg]$, as the two-process model predicts. Stronger tests of the two-process model can be obtained by focusing on subsets of disk stars with the highest-S/N spectra, so that the observational contributions to scatter

are all minimized. We reserve such an investigation for future work.

5. IMF Constraints

Recent works by Ballero et al. (2007) and Grieco et al. (2012, 2015) find that the bulge (and galactic center) is better fit by a chemical evolution model with a more top-heavy IMF than that which fits the solar neighborhood. Grieco et al. (2012) employed chemical evolution modeling to reproduce the metal-rich and metal-poor bulge populations. They found that a model with a flatter IMF, such as the Salpeter (1955), fits the MDF and $[Mg/Fe]$ versus $[Fe/H]$ abundance distribution of blue red clump stars from Hill et al. (2011).

Our measurements allow an entirely different test of IMF differences between the bulge and the disk because the relative amounts of different elements produced in a CCSN depend on the mass of the progenitor. Changing the high-mass slope of the IMF will increase or decrease the number of massive stars and thus the ratio of nucleosynthetic products from the IMF integrated CCSN population. If a steeper or shallower IMF induces larger abundance differences than those observed, we can exclude that possible IMF in the bulge.

We adopt a Kroupa IMF (Kroupa 2001) as our standard for the disk. This three-slope IMF is shown in Equation (9), with $a_3 = -2.3$. To produce a top-heavy or -light IMF, we change the high-mass slope (a_3) to -2.0 or -2.6 , respectively. Our

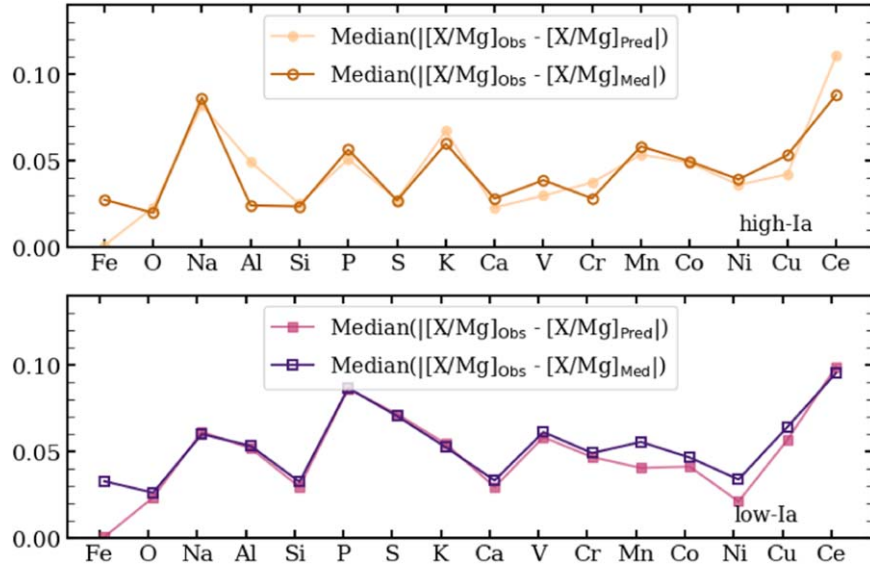


Figure 11. Median absolute difference of the observed bulge stars’ $[X/Mg]$ (including offsets) and the predicted $[X/Mg]$ values for high-Ia (light orange; top) and low-Ia (pink; bottom) populations. Alongside, we plot the median absolute difference of the observed bulge stars’ $[X/Mg]$ and the median $[X/Mg]$ value binned by $[Mg/H]$ on the high-Ia (dark orange; top) or low-Ia (purple; bottom) populations. Only stars with $Mg/H > -0.7$ are included in the calculations.

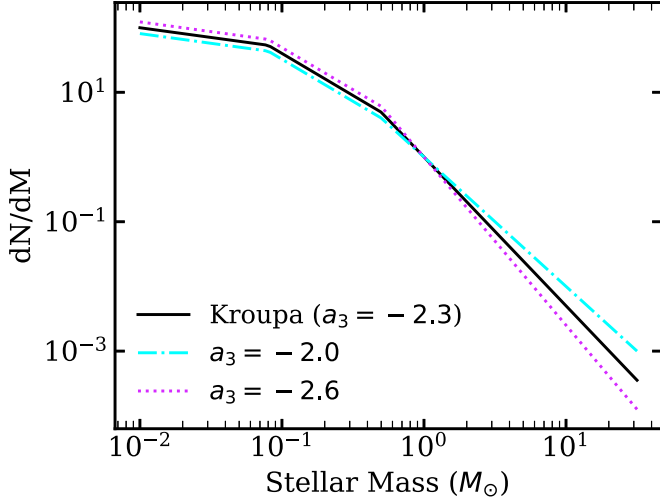


Figure 12. Kroupa IMF (black) and edited Kroupa IMFs with high-mass slopes of -2.0 (cyan) and -2.6 (pink). We compare the resulting yields of populations integrated under these three IMFs.

IMFs are all of the form

$$\frac{dN}{dM} = \begin{cases} A_K M^{-0.3}, & M < 0.08 \\ B_K M^{-1.3}, & 0.08 \leq M < 0.5, \\ C_K M^{a_3}, & M \geq 0.5 \end{cases} \quad (9)$$

with A_K , B_K , and C_K being the appropriate multiplicative constants. The three IMFs are plotted in Figure 12.

To derive the CCSN abundance yields from our three IMFs, we employ the Versatile Integrator for Chemical Evolution (VICE) and its yield integration function (Johnson & Weinberg 2020). In our analysis, we take net CCSN yields from Chieffi & Limongi (2013, hereafter CL13) at solar metallicity. While CL13 exploded all stars to $120 M_\odot$, we assume for our modeling that progenitors above $30 M_\odot$ collapse to black holes instead of exploding as CCSNe. This sharp cutoff is a simplification of an “explodability landscape” that is probably much more complex (Pejcha & Thompson 2015; Sukhbold et al. 2016). The VICE

integrator returns yields in solar mass of element X per M_\odot of stars formed. We convert to bracket notation using solar abundances from Asplund et al. (2009). We note that APOGEE takes solar abundances from Grevesse et al. (2007), but we do not expect this to impact our results.

The resulting yields and $[X/Mg]$ integrated with all three IMFs can be found in Table 4 of Appendix C. This appendix includes a more detailed exploration of the CL13 yields, such as their sensitivity to metallicity and to the choice of upper mass cutoff for explosion. We also include a similar calculation for the Limongi & Chieffi (2018, hereafter LC18) yields, which explode stars to $25 M_\odot$ with different explosion criteria. We note that the CL13 yields force an ejection of $0.1 M_\odot$ of ^{56}Ni from all stars. We also include a similar calculation for the Limongi & Chieffi (2018, hereafter LC18) yields, which explode stars to $25 M_\odot$ with different explosion criteria in Table 5 of Appendix C.

Unfortunately, while the predicted yields are mass-dependent, that dependence is fairly similar for all of the elements examined here. As a result, the theoretical $[X/Mg]$ abundances for the Kroupa and $a_3 = -2.0$ or $a_3 = -2.6$ IMFs differ by small amounts, 0.05 dex for $[\text{Ni}/\text{Mg}]$ and 0.01–0.02 dex for other elements. These IMF-induced abundance differences are plotted in Figure 13. Taking Kroupa as the standard, we show the $\Delta[X/Mg]$ values for 12 elements, where

$$\Delta[X/Mg] = [X/Mg]_{\text{Kroupa}} - [X/Mg]_{a_3=-2.0} \quad (10)$$

or

$$\Delta[X/Mg] = [X/Mg]_{\text{Kroupa}} - [X/Mg]_{a_3=-2.6}. \quad (11)$$

Although these values are plotted as horizontal lines, they are calculated at solar $[\text{Fe}/\text{H}]$. We stress that this calculation only investigates star formation changes that would affect the CCSN contribution to each element. We do not account for any differences in SN Ia nucleosynthesis between the bulge and disk at fixed $[Mg/H]$ and $[\text{Fe}/\text{Mg}]$. A difference in SN Ia-produced $[X/\text{Fe}]$ ratios could compensate for or masquerade as an IMF-induced change to CCSN contributions.

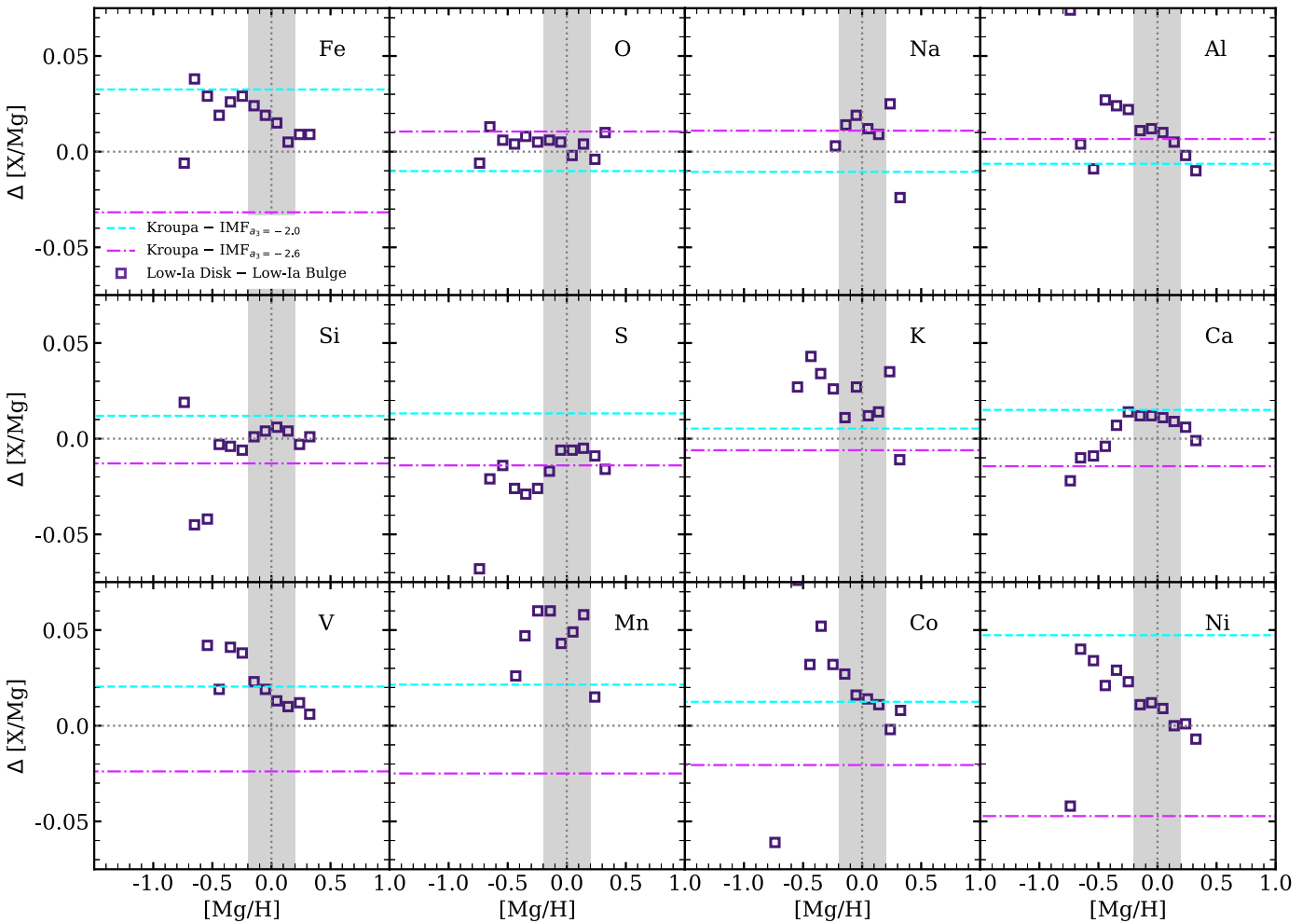


Figure 13. Differences between the bulge and resampled disk low-Ia median sequences (purple squares) and theoretical abundance changes between the standard Kroupa IMF ($a_3 = -2.3$) and a Kroupa IMF with an altered high-mass slope. The induced elemental differences between the Kroupa and $a_3 = -2.0$ IMFs are shown with the cyan dashed lines and those for $a_3 = -2.6$ with the magenta dashed-dotted lines. The theoretical and observed abundances should be compared near solar $[\text{Mg}/\text{H}]$, as indicated by the gray band.

For comparison, Figure 13 also shows the observed differences in the bulge and resampled disk low-Ia median points,

$$\Delta[X/\text{Mg}] = [X/\text{Mg}]_{\text{disk}} - [X/\text{Mg}]_{\text{bulge}}. \quad (12)$$

We compare only the low-Ia median abundances, as the bulge low-Ia sequence is better populated than the high-Ia sequence, and we wish to minimize the SN Ia contribution for this test in any case. We have already seen in Figure 8 that the disk and bulge median sequences agree well, and in Figure 13, we see that the differences near solar metallicity are typically 0.02 dex or below. These are comparable in magnitude to the predicted IMF effects, but some elements agree better with the steeper IMF and some with the shallower IMF, with no clear pattern to separate these groups. We are therefore inclined to ascribe these differences to residual systematics in matching disk and bulge abundance scales at the 0.02 dex level.

Two elements deserve special mention. The $[\text{Mn}/\text{Mg}]$ ratios show the largest differences between disk and bulge, ~ 0.05 dex, much larger than predicted by an IMF change. If real, this difference likely arises from different SN Ia enrichment in the bulge, perhaps connected to the strong apparent metallicity dependence of Mn yields. The $[\text{Ni}/\text{Mg}]$

ratios, on the other hand, show 0.01 dex agreement near solar metallicity, much closer than the 0.04 dex changes predicted by the IMF models. At face value, this comparison implies a stringent limit on IMF differences, with $|\Delta a_3| \lesssim 0.1$. However, Ni predictions may be sensitive to the criteria used to define the mass cut in SN models. Ideally, we would like to base an IMF test on relative abundances of Mg, O, Si, and Ca, which are well measured and predicted (and empirically inferred) to come predominantly from CCSNe with little metallicity dependence. If abundance scales of different populations can be reliably cross-calibrated at the 0.01 dex level, then tests of IMF variations at the $|\Delta a_3| \approx 0.2\text{--}0.3$ level can be achieved.

6. Summary

Using APOGEE DR16+ data, we present the $[X/\text{Mg}]$ versus $[\text{Mg}/\text{H}]$ and $[X/\text{Fe}]$ versus $[\text{Fe}/\text{H}]$ abundance trends of the Milky Way bulge ($R < 3$ kpc) for Fe, O, Na, Al, Si, P, S, K, Ca, V, Cr, Mn, Co, Ni, Cu, and Ce, the latter two being new to DR16. The addition of the LCO instrument in APOGEE DR16 provides us with observations of stars in the southern hemisphere and thus a more complete look at the bulge than previous APOGEE data releases. After a series of quality cuts, we are left with 11,229 bulge stars with a median S/N of 149.

Like the disk, the bulge population shows a bimodal [Mg/Fe] versus [Fe/H] distribution. The DR16+ data reveal that the two populations are distinct and do not form a continuous sequence. As in W19, we divide the sample into high- and low-Ia populations in this plane. We see median [Mg/Fe] versus [Fe/H] trends that match those of the W19 disk definition, though slightly offset. As in Hayden et al. (2015) and W19, we find that the inner Galaxy contains more low-Ia stars than high-Ia stars, with the stellar distribution extending to an [Fe/H] of -1.5 .

In Section 3, we present the [X/Mg] versus [Mg/H] and [X/Fe] versus [Fe/H] abundance distributions and the [X/Mg] versus [Mg/H] median trends for the APOGEE elements. Some data systematics can be seen, including a fingerlike feature in low-Ia O, Ca, and Si in [X/Fe] space; a bimodal distribution of high-Ia Cr stars; and banding/clumping in the Al, P, and V abundance distributions. We only exclude the lower [Cr/Mg] high-Ia stars in our analysis, but we explore the impact of these systematics in Appendix A.

The main goal of this paper is to determine the similarity or dissimilarity between the median high- and low-Ia [X/Mg] trends of the Galactic bulge and disk. However, upon a comparison of our bulge sample with the disk as defined by W19, we find systematic abundance differences that correlate with the stellar $\log(g)$ distribution. We therefore resample the APOGEE DR16+ disk to select a subset of stars that reproduce the $\log(g)$ distribution of the bulge. We divide the resampled disk stars into high- and low-Ia populations.

The similarities between the median high- and low-Ia trends of the bulge and disk shown in Figure 8 are striking. All elemental trends agree to within 0.1 dex and most within 0.05 dex; near solar [Mg/H], the agreement of the low-Ia median trends is typically 0.01–0.02 dex (Figure 13). The [Na/Mg] and [Mn/Mg] versus [Mg/H] bulge high-Ia median trends rise more steeply than those of the disk. The low-Ia [Mn/Mg] median trend is about 0.05 dex higher in the bulge than the disk. The Co bulge medians are offset to lower [Co/Mg] than the resampled disk at low [Mg/H]. These differences could reflect differences in the chemical evolution of the disk and bulge, but they are small enough that they could still reflect an imperfect relative calibration of the bulge and disk abundance scales.

This close agreement of median [X/Mg] trends between the bulge and disk extends the universality of these trends as a function of R and $|Z|$ within the disk found by W19. It demonstrates that although the distribution of stars in [Mg/H] and [Fe/Mg] depends strongly on location in the Galaxy, the physics that determines [X/Mg] ratios for a given [Mg/H] and [Fe/Mg] does not. To quantify this point, we compare the observed bulge abundance ratios with those predicted by W19’s empirical two-process model fit to the resampled disk. The two-process model describes the abundances of a star or population of stars as the sum of prompt (CCSN) and delayed (SN Ia) components, with each of these contributions to (X/Mg) having a power-law dependence. Using the parameters derived as the best fit to the resampled disk’s median abundances for each element (R_{Ia}^X , α_{cc} , and α_{Ia}), we predict the bulge elemental abundances suite based only on the observed [Fe/Mg] and [Mg/H] of the bulge stars. Figure 10 shows that the predicted abundances accurately trace the observed [X/Mg] median trends. Elements for which the predicted and observed trends diverge show poor two-process

model fits (e.g., Al) and/or real differences in the median trends of the bulge and resampled disk (e.g., Na, Mn, Co). Star-by-star deviations from median trends appear to be dominated by observational errors, but the two-process model explains a small fraction of the scatter for some iron-peak elements.

As prior works have supported a bulge IMF with a shallower high-mass slope than the solar neighborhood (Grieco et al. 2012), we test whether the bulge and sampled disk’s similar abundance tracks can constrain the Galactic IMF variability. Using the yield integration function of VICE (Johnson & Weinberg 2020), we calculate the theoretical [X/Mg] abundance at solar [Fe/H] for the CL13 yields with three IMFs: Kroupa with high-mass slopes of -2.0 , -2.3 , or -2.6 . Overall, we find small predicted [X/Mg] changes with a varying IMF, <0.05 dex for all elements. If the bulge and disk have different IMFs, we would expect the median abundance differences of the bulge and resampled disk to correlate with the theoretical abundance changes induced by an altered IMF. However, we do not see consistent agreement between the observed and theoretical $\Delta[X/Mg]$ trends for either IMF variation (Figure 13). The observed agreement of median trends argues against IMF slope differences larger than about 0.3. At face value, the agreement for [Ni/Mg] implies a more stringent limit, but the predicted sensitivity of Ni yields to the IMF may not be robust. The 0.05 dex difference in [Mn/Mg] trends could be a sign of differences in SN Ia enrichment between bulge and disk.

Our principal finding is that the bulge and resampled disk have similar [X/Mg] versus [Mg/H] median abundance tracks, extending the conclusions of Hayden et al. (2015) and W19 to the inner Galaxy. The universality of the median [X/Mg] abundance trends suggests that they are not sensitive to most aspects of chemical evolution and instead depend on the IMF-averaged nucleosynthetic yields, which appear consistent throughout the Galaxy. As we obtain additional high-S/N observations of the Milky Way bulge, our understanding of Galactic nucleosynthetic processes will grow. In future works with APOGEE and other data sets, we aim to set more stringent empirical constraints on the astrophysics that governs the creation of the elements throughout the Galaxy and its closest neighbors.

We thank APOGEE collaborators Julie Imig, Jianhui Lian, Steve Majewski, Matthew Shetrone, and Gail Zasowski, who were in attendance at the autumn 2019 OSU and bulge workshops and provided many insights on APOGEE abundances and findings for the bulge. We thank the Center for Cosmology and AstroParticle Physics for helping to organize the autumn 2019 OSU workshop.

E.G., D.H.W., J.A.J., and J.W.J. acknowledge supported from NSF grant AST-1909841. D.A.G.H. acknowledges support from the State Research Agency (AEI) of the Spanish Ministry of Science, Innovation and Universities (MCIU) and the European Regional Development Fund (FEDER) under grant AYA2017-88254-P. S.H. is supported by an NSF Astronomy and Astrophysics Postdoctoral Fellowship under award AST-1801940. H.J. acknowledges support from the Crafoord Foundation, Stiftelsen Olle Engkvist Byggmästare, and Ruth och Nils-Erik Stenbäcks stiftelse. D.M.N. acknowledges support from NASA under award No. 80NSSC19K0589. A.R.-L. acknowledges financial support provided in Chile by Comisión Nacional de Investigación Científica y Tecnológica

(CONICYT) through FONDECYT project 1170476 and by QUIMAL project 130001.

Funding for the Sloan Digital Sky Survey IV has been provided by the Alfred P. Sloan Foundation, the U.S. Department of Energy Office of Science, and the Participating Institutions. SDSS-IV acknowledges support and resources from the Center for High-Performance Computing at the University of Utah. The SDSS website is www.sdss.org.

SDSS-IV is managed by the Astrophysical Research Consortium for the Participating Institutions of the SDSS Collaboration, including the Brazilian Participation Group, the Carnegie Institution for Science, Carnegie Mellon University, the Chilean Participation Group, the French Participation Group, the Harvard-Smithsonian Center for Astrophysics, Instituto de Astrofísica de Canarias, The Johns Hopkins University, the Kavli Institute for the Physics and Mathematics of the Universe (IPMU)/University of Tokyo, the Korean Participation Group, Lawrence Berkeley National Laboratory, Leibniz Institut für Astrophysik Potsdam (AIP), Max-Planck-Institut für Astronomie (MPIA Heidelberg), Max-Planck-Institut für Astrophysik (MPA Garching), Max-Planck-Institut für Extraterrestrische Physik (MPE), National Astronomical Observatories of China, New Mexico State University, New York University, the University of Notre Dame, Observatório Nacional/MCTI, The Ohio State University, Pennsylvania State University, Shanghai Astronomical Observatory, the United Kingdom Participation Group, Universidad Nacional Autónoma de México, the University of Arizona, the University of Colorado Boulder, the University of Oxford, the University of Portsmouth, the University of Utah, the University of Virginia, the University of Washington, the University of Wisconsin, Vanderbilt University, and Yale University.

This research made use of Astropy,¹⁸ a community-developed core Python package for astronomy (Astropy Collaboration et al. 2013, 2018).

Software: VICE (Johnson & Weinberg 2020), Astropy (Astropy Collaboration et al. 2013, 2018).

Appendix A

The Effect of Data Systematics on Median Trends

In Section 3, we present the median high- and low-Ia abundance trends for APOGEE elements and discuss some of the systematics and artifacts afflicting the data in Section 3.1. In the $[X/Fe]$ versus $[Fe/H]$ plots (Figure 3), we see a fingerlike feature in O, Ca, and Si; bimodality in the Cr high-Ia stars; banding in Al and P; and a clump in V. In our data analysis, we exclude some stars to mitigate the Cr feature and proceed with the other artifacts included. Here we take a closer look at these anomalies to see how the median trends change with their inclusion and exclusion.

Figure 14 presents three versions of the $[Cr/Mg]$ median high-Ia trend. The first panel shows the observed distribution with no cuts. The high-Ia median trend follows the Cr-poor stars at low $[Mg/H]$ but jumps to solar $[Cr/Mg]$ around $[Mg/H] \sim 0.3$. The bimodality in the Cr abundance obviously produces a skewed median trend. In our analysis, we remove 1421 stars with $0 < [Mg/H] < 0.75$ and $-0.3 < [Cr/Mg] < -0.1$. This exclusion and the resulting median high-Ia trend are shown in the middle panel of Figure 14. Alternatively,

we could have excluded the 1544 Cr-rich stars with $0 < [Mg/H] < 0.75$ and $-0.1 < [Cr/Mg] < 0.2$, as shown in the right panel. As expected, the high-Ia median trend changes dramatically between the two exclusions. The higher $\log(g)$ disk better resembles the Cr-rich high-Ia stars and previous works, so we use this subset in our analysis.

While we mitigate the Cr systematic with exclusions in our data analysis, the α finger and other banding/clumping are left in. Figures 15 and 16 show examples of how the $[Ca/Mg]$ and $[Al/Mg]$ versus $[Mg/H]$ trends (respectively) would change if we removed these features. For Ca, we isolate the finger stars in $[Ca/Fe]$ versus $[Fe/H]$ space, where the finger is much easier to identify. We define the finger as low-Ia stars with $-0.3 < [Fe/H] < 0.5$ and $0.15 < [Cr/Fe] < 0.3$. Median trends including and excluding these stars are plotted in the right panel of Figure 15. The low-Ia median trend changes insignificantly after the exclusion of 368 finger stars. We find that the inclusion of the bulge finger stars in our O, Si, and Ca analysis does not affect our resulting median trends or conclusions.

The low abundance trends (J20) seen in Al and P are much harder to isolate, as they blend into the main abundance tracks. The left panel of Figure 16 plots $[Al/Fe]$ versus $[Fe/H]$, where the banding is more pronounced than in Mg space. We define two exclusion regions. The first (1) is $[Al/Fe] < 0.05$ and $[Fe/H] < 0.1$ for low-Ia stars, and the second (2) is $-0.1 < [Al/Fe] < -0.3$ and $-0.2 < [Fe/H] < 0.7$ for high-Ia stars. Both boxes are drawn on the figure and include 2700 and 206 stars, respectively. Median trends including and excluding these stars are shown in the right panel. The high-Ia trend is not noticeably affected by the small exclusion, but the low-Ia trend deviates from the full population median at low $[Mg/H]$. This deviation should be expected, as we cut out many of the low- $[Mg/H]$ stars. While the Al “tail” may be a systematic, the median trends above $[Mg/H] = -0.25$ are robust. As the bulge and disk median trends agree at this metallicity, our conclusions about the similarity of the bulge and disk abundance ratios hold.

We also explore the temperature correlation of the median abundance trends. As noted in Section 3, APOGEE flags low-temperature Na, K, and Mn stars due to reduction systematics that correlate with temperature. To see if this affects the median high- and low-Ia trends, we compare the full sample medians to those of smaller temperature divisions. Figure 17 plots $[Na/Mg]$ versus $[Mg/H]$ distributions and medians for a sample with no temperature cuts, stars with $3800 \text{ K} \leq T_{\text{eff}} < 4200 \text{ K}$ (2800), and stars with $4200 \text{ K} \leq T_{\text{eff}} < 4600 \text{ K}$ (931). The majority of stars lie within the lower-temperature range, so the medians of this sample track the full population. Both median sequences of the higher-temperature sample lie below those of the full population, though the differences are < -0.05 dex. The median high- and low-Ia Na trends appear to have some small correlation with temperature.

We repeat this analysis with all other elements using the same temperature divisions. In most cases, the lower-temperature bin dominates the sample and agrees well with the full population medians. We see no temperature-dependent changes in the $[X/Mg]$ versus $[Mg/H]$ median trend location for Ca, K, Mn, Ni, Cu, and Ce. In the higher-temperature bin, we find that the low-Ia trends of Al, O, and Si sit slightly above the full population medians, and those of Co and Cr sit below (in many cases, there are too few high-Ia median points to draw strong

¹⁸ <http://www.astropy.org>

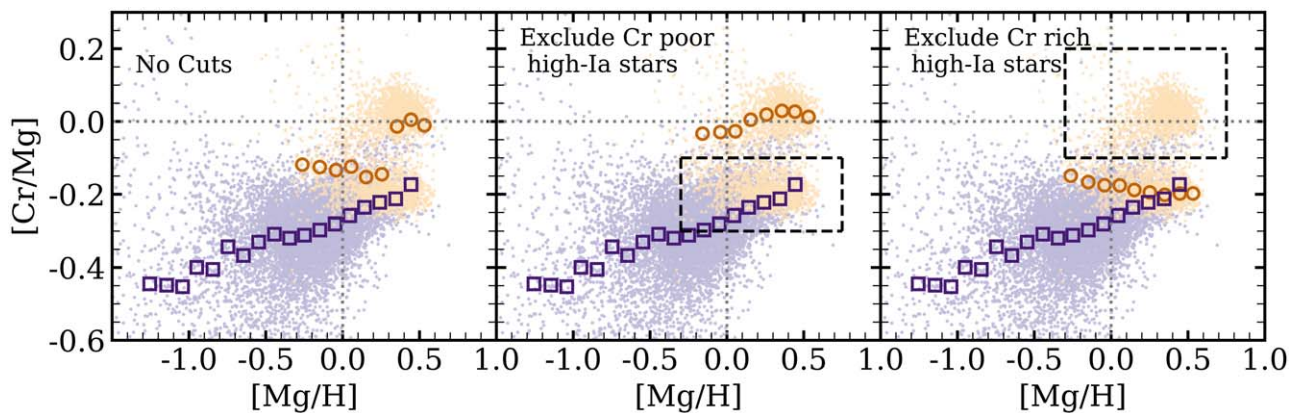


Figure 14. Bulge $[\text{Cr}/\text{Mg}]$ vs. $[\text{Mg}/\text{H}]$ distribution with high-Ia stars in orange and low-Ia stars in purple. The medians of the high-/low-Ia populations are overplotted in orange/purple circles/squares, where we bin by 0.1 dex and require >20 stars per bin. Left: median trends for the full population. Middle: median trends excluding the Cr-poor high-Ia stars inside the dashed box (exclusion employed in the main body of the paper). Right: median trends excluding the Cr-rich high-Ia stars inside the dashed box.

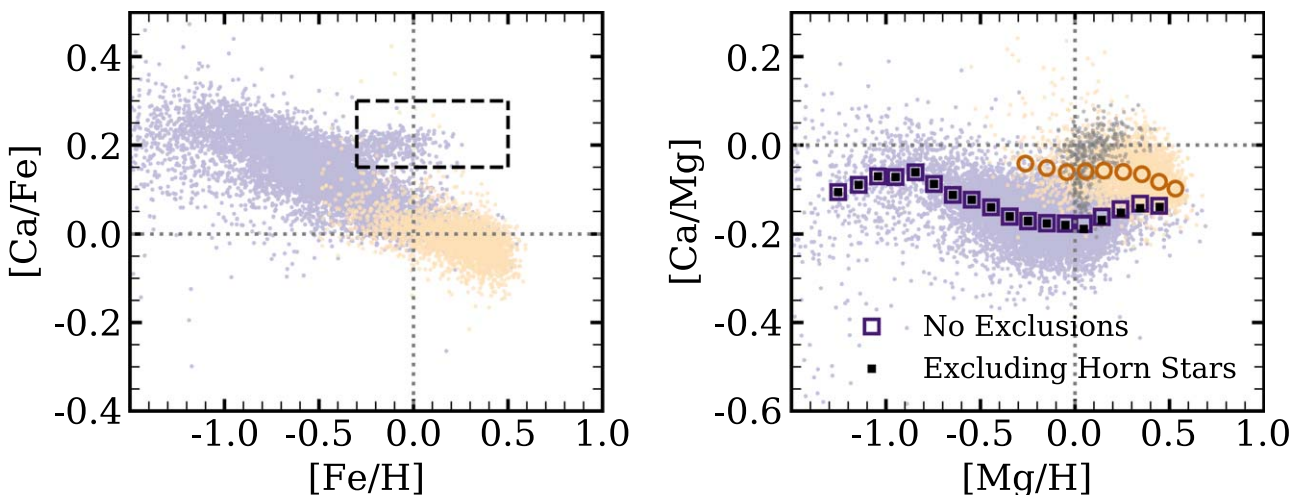


Figure 15. Left: bulge $[\text{Ca}/\text{Fe}]$ vs. $[\text{Fe}/\text{H}]$ distribution with high-Ia stars in orange and low-Ia stars in purple. The overplotted dashed box identifies the finger stars. Right: $[\text{Ca}/\text{Mg}]$ vs. $[\text{Mg}/\text{H}]$ distribution. The medians of the full high-/low-Ia populations are overplotted in orange/purple circles/squares, where we bin by 0.1 dex and require >20 stars per bin. The black squares show the resulting low-Ia median trend when we exclude the finger stars (shown in gray).

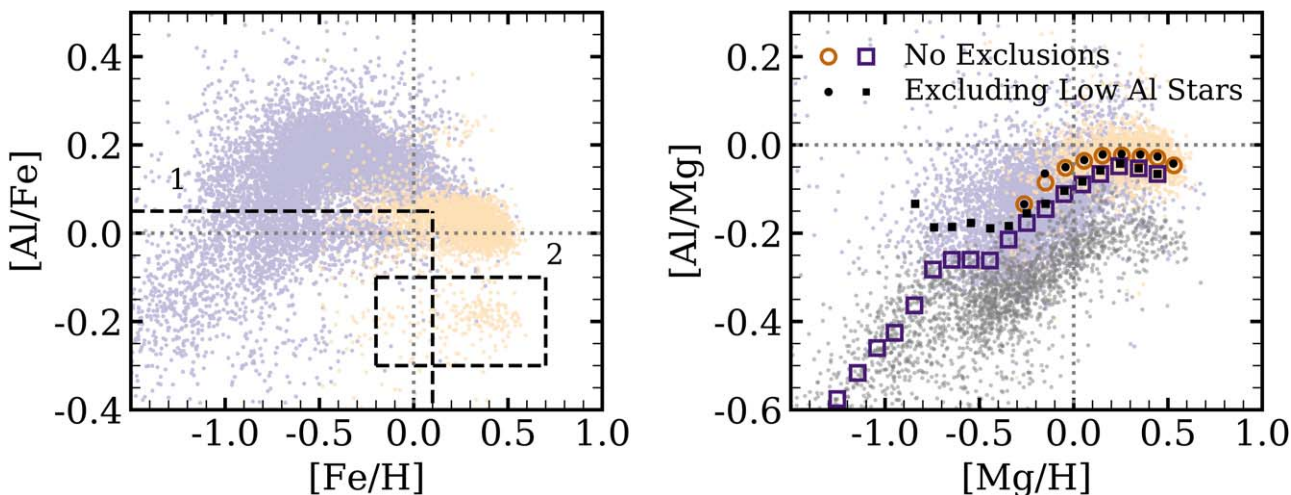


Figure 16. Same as Figure 15 but for Al. In the left panel, exclusion region 1 (2) applies to the low-Ia (high-Ia) stars. All excluded stars are shown in gray in the right panel.

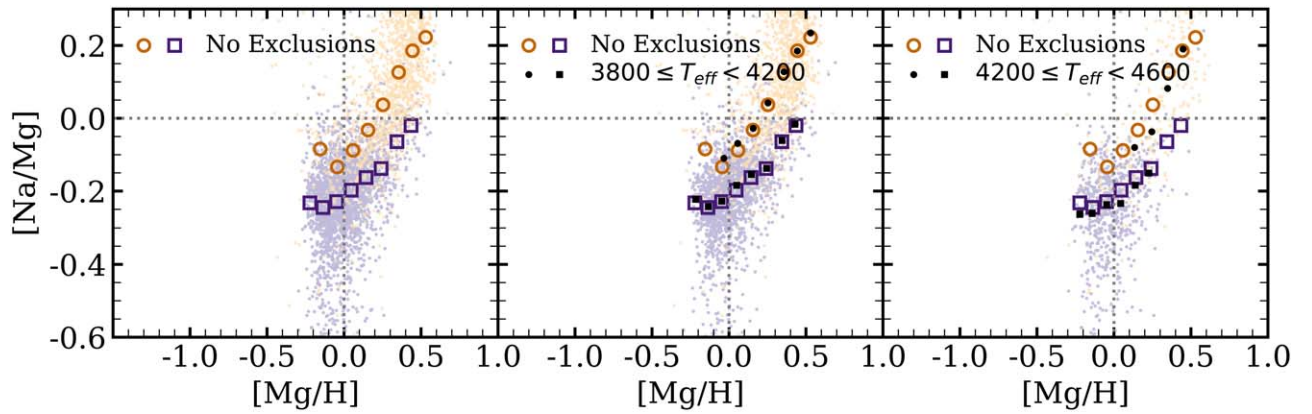


Figure 17. Bulge $[\text{Na}/\text{Mg}]$ vs. $[\text{Mg}/\text{H}]$ distribution with high-Ia stars in light orange and low-Ia stars in light purple. The medians of the full high-/low-Ia populations are overplotted in dark orange/purple circles/squares, where we bin by 0.1 dex and require >20 stars per bin. Left: full sample (3851 stars) These medians remain the same in each panel. Middle: medians of stars with $3800 \text{ K} \leq T_{\text{eff}} < 4200 \text{ K}$ (2800 stars). Medians of the full population are in orange/purple, and those of the temperature cut sample are in black. The background light orange/purple points show the subsample of stars in the temperature range. Right: same as middle panel but for stars with $4200 \text{ K} \leq T_{\text{eff}} < 4600 \text{ K}$ (931 stars) in black.

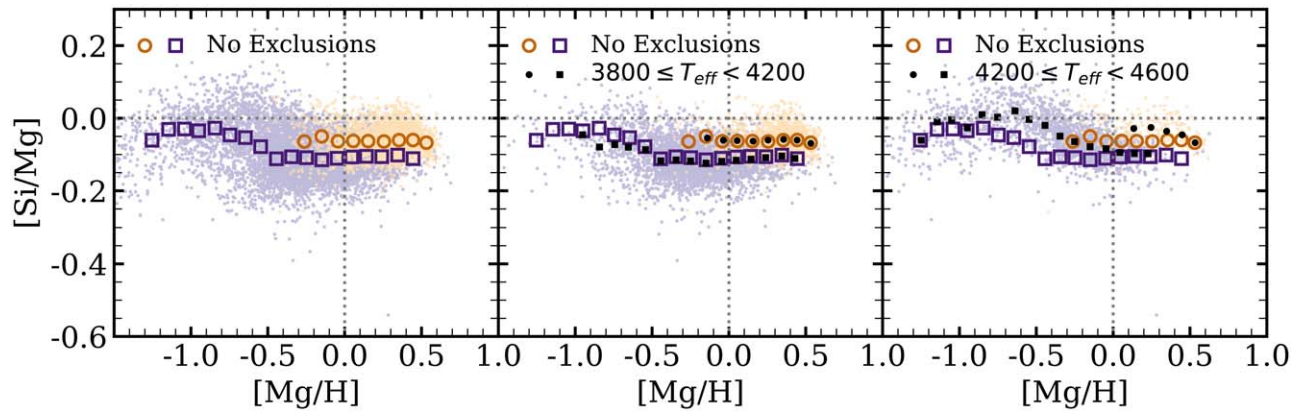


Figure 18. Same as Figure 17 but for Si. There are 5254 stars in the lower-temperature range and 2208 in the higher-temperature range.

conclusions). The Si displays one of the largest low-Ia median trend changes in the higher-temperature bin (~ 0.1 dex), shown in Figure 18. Some elemental abundance variations with temperature, such as Si, are on the scale of or larger than the difference between the bulge and disk medians.

While we match $\log(g)$ distributions between the bulge and disk samples, we do not match T_{eff} distributions. To verify that our conclusions hold, we check the median high- and low-Ia disk trends’ variation with temperature. We find similar deviations in the disk as in the bulge; e.g., the median Si high- and low-Ia trends of stars with $4200 \text{ K} \leq T_{\text{eff}} < 4600 \text{ K}$ in the disk lie above those of the full population by a similar amount to that seen in Figure 18. While there is uncertainty in the exact location of the abundance trends, we have confidence that the bulge and disk trends agree.

Appendix B Cu and Ce Abundances

While the main body of this paper focuses on the abundance trends in the Milky Way bulge, in this appendix, we will take a closer look at the disk Cu and Ce abundances, continuing the work of W19 and GJW for the two new APOGEE elements. In Figure 19, we plot the Cu and Ce abundances for all stars using

the W19 disk sample cuts ($1 < \log(g) < 2$, $3700 \text{ K} < T_{\text{eff}} < 4600 \text{ K}$, $3 \text{ kpc} < R < 15 \text{ kpc}$, $|Z| < 2 \text{ kpc}$) with median high- and low-Ia trends (calculated as in Section 3). Overplotted are the GALAH median high- and low-Ia trends for Cu and La from GJW.

The APOGEE and GALAH Cu abundances agree reasonably well above solar $[\text{Mg}/\text{H}]$. Here both surveys’ $[\text{Cu}/\text{Mg}]$ median trends show large sequence separation and positive slopes. The GALAH medians are significantly more inclined, especially when comparing the high-Ia sequences. As noted in Section 3.4, the APOGEE Cu abundances turn upward toward higher $[\text{Cu}/\text{Mg}]$ at low $[\text{Mg}/\text{H}]$. We do not trust the measurements for low- $[\text{Mg}/\text{H}]$ stars.

As GALAH does not report Ce abundances, we first compare Ce to La, the closest observed element on the periodic table with similar neutron-capture origins. Both elements show the expected nonlinear trends. In Ce and La, we see a clear peak in the high-Ia median trends near solar. The same is seen in the low-Ia medians, though the Ce peak is smaller and offset to higher $[\text{Mg}/\text{H}]$ (we ignore the upturned low-Ia tail at low $[\text{Mg}/\text{H}]$, as there are fewer stars here). As explained in GJW, the trends rise with $[\text{Mg}/\text{H}]$ in the low-metallicity regime because of the increasing numbers of Fe seeds and then decline

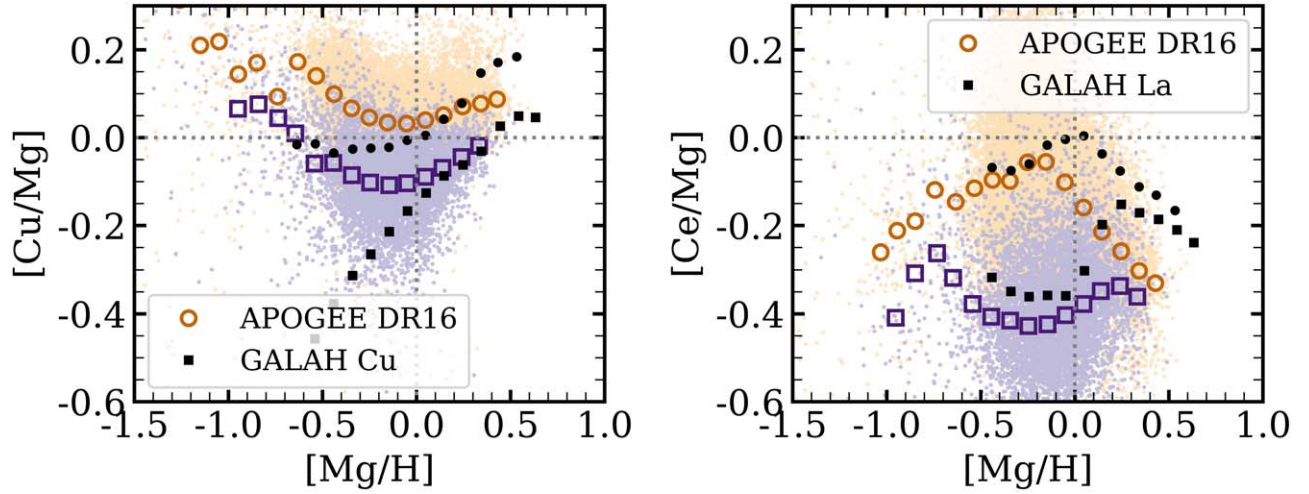


Figure 19. APOGEE [Cu/Mg] (left) and [Ce/Mg] (right) vs. [Mg/H] abundances for the W19 disk, with high-Ia stars in light orange and low-Ia stars in light purple. The medians of the high- and low-Ia populations are overlotted with dark orange circles and dark purple squares, respectively. GALAH high-Ia (black circles) and low-Ia (black squares) medians from GJW are also included for [Cu/Mg] (left) and [La/Mg] (right; GJW).

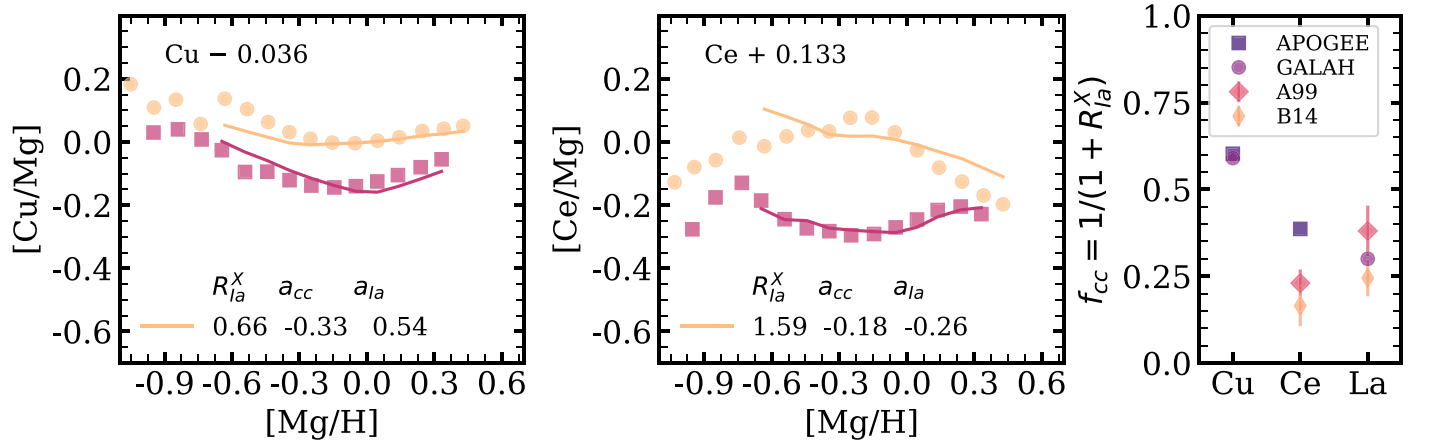


Figure 20. Left: same as Figure 9 but for Cu abundances in a sample with the W19 disk cuts. Middle: same for Ce abundances. Right: fractional CCSN contribution to Cu, Ce, and La as calculated from R_{Ia}^X values for fits to APOGEE (dark purple squares) and GALAH (light purple circles). Theoretical r -process contributions from Arlandini et al. (1999, A99; pink diamonds) and Bisterzo et al. (2014, B14; orange diamonds) are included for Ce and La.

with [Mg/H] in the high-metallicity regime because of the decreasing neutron-to-seed ratio (Gallino et al. 1998).

We further compare APOGEE Ce abundances with other high-resolution, high-S/N studies from Battistini & Bensby (2016; 361 dwarf stars in the solar neighborhood) and Delgado Mena et al. (2017; 1012 dwarf stars from the HARPS-GTO survey). We divide the high- and low-Ia stars according to Equation (1) and bin the median points by 0.1 dex in [Mg/H]. We see an agreement between APOGEE and both studies. The smaller data set from Battistini & Bensby (2016) shows a declining high-Ia trend and a flat low-Ia trend near solar, in agreement with APOGEE data. The Delgado Mena et al. (2017) Ce abundances also appear in agreement with APOGEE, though the trends are offset to higher [Ce/Mg]. Neither study includes sufficient high-Ia stars with [Mg/H] < 0.04 to identify the high-Ia peak seen in APOGEE. We also refer the reader to Jönsson et al. (2020, Figure 14), who compared APOGEE DR16 Ce abundances with those of high-resolution bulge giants from Forsberg et al. (2019) and found reasonable agreement between the two surveys. Conclusions from APOGEE’s Ce trends, however, should be drawn with caution, as they are derived from a single line and prone to large uncertainties.

We fit both the [Cu/Mg] and [Ce/Mg] disk median trends with the two-process model, as outlined in Section 4 (Figure 20). As

both elemental trends are nonlinear, the two-process model does not reproduce observations at the low-metallicity end. However, it does give us a sense of the sequence separation at [Mg/H] = 0. It was found by GJW that Cu has $R_{\text{Ia}}^X = 0.71$, $\alpha_{\text{cc}} = 0.56$, and $\alpha_{\text{Ia}} = -0.40$. The α_{cc} and α_{Ia} values found for APOGEE differ drastically (likely due to the upturn at low metallicity), but the R_{Ia}^X value of 0.66 is in good agreement with GALAH. APOGEE’s R_{Ia}^X for Ce and GALAH’s La differ more, at 1.59 and 2.31, respectively. The α_{cc} and α_{Ia} terms hold less meaning, as the abundance tracks do not follow a power-law dependence.

In the right panel of Figure 20, we plot the f_{cc} values corresponding to all four R_{Ia}^X measurements. The GALAH and APOGEE points for Cu overlap around $f_{\text{cc}} = 60\%$, showing a strong agreement that Cu has a large delayed component. As detailed in GJW, this component may be due to AGB stars, as SN Ia models do not produce substantial amounts of Cu. For Ce and La, the f_{cc} value is better interpreted as a fractional r -process component (f_r). APOGEE and GALAH find Ce and La, respectively, to have around 30%–40% r -process contribution. We note that our two-process models are scaled to CCSNe and SNe Ia, so this estimated percentage could change if the s -process and SN Ia enrichment have different delay times. The f_r values for our neutron-capture elements agree

reasonably well with theory, which predicts both to be s -process-dominated. Arlandini et al. (1999) found Ce to have 77% s -process contribution (f_s), and Bisterzo et al. (2014) found 83%. See GJW for a broader discussion of La. Figure 20 plots these theoretical f_r values for both elements, taking $f_r = 1 - f_s$.

Appendix C CCSN Yield Exploration

In Section 5, we present the theoretical $[X/Mg]$ abundances at solar $[Fe/H]$ as calculated from the net CL13 yields integrated with three different IMF high-mass slopes. In this appendix, we provide additional information about the net CL13 and LC18 CCSN yields and their resulting $[X/Mg]$ abundances. While LC18 cited multiple improvements to

the CL13 approach, we note differences in their explosion criterion: CL13 imposed a mass cut that ejects $0.1 M_\odot$ of ^{56}Ni for all stars, while LC18 set interior $[\text{Ni}/\text{Fe}]$ values and chose a mass cut that ejects $0.07 M_\odot$ of ^{56}Ni for stars with $M \leq 25 M_\odot$. Both compute yield calculations for rotating stars, but we do not explore rotation effects here.

The foundation of our earlier IMF investigation rests on the fact that CCSN yields have a mass dependence. If the high-mass IMF slope steepens/flattens, then the Galaxy sees fewer/more high-mass stars and their nucleosynthetic products. The IMF integrated abundances shown above (and given in Tables 4 and 5) are thus dependent upon the elemental yield's mass dependence. In our case, we need to know how the yields vary relative to Mg. Figure 21 shows the net Mg and X/Mg yields for O, Al, Si, Ca, and Ni as a function of mass for CL13

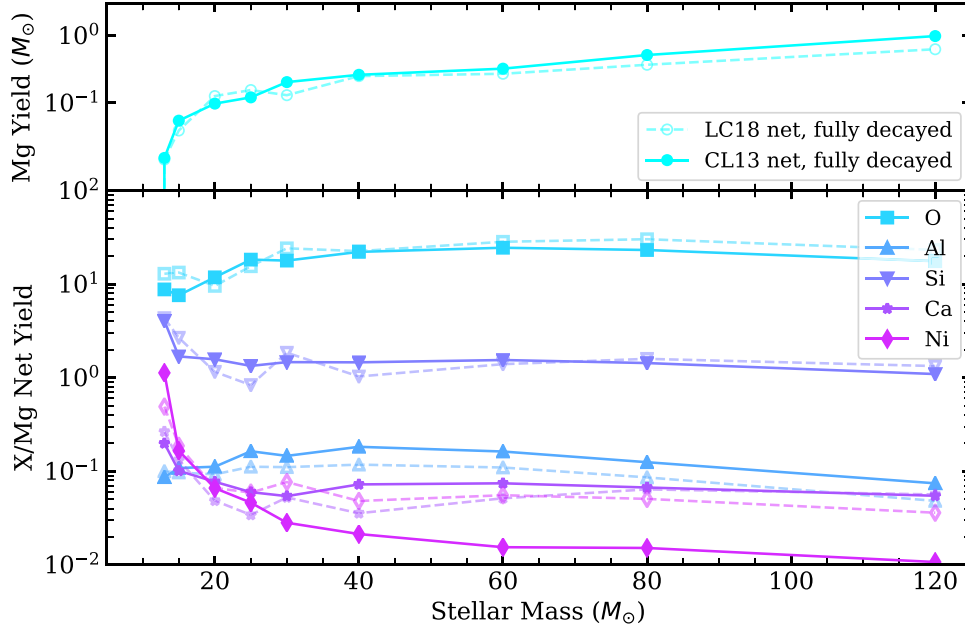


Figure 21. Elemental net yields from CL13 (solid) and LC18 (dashed) as a function of mass for $[Fe/H] = 0$ with no rotation. Top: net explosive and wind Mg yields in M_\odot (cyan circles) for published CL13 (filled circles and solid line) and unpublished LC18 (open circles and dashed line). Both are reported after a full decay of unstable isotopes. Bottom: net X/Mg yields for O (light blue squares), Al (dark blue upward triangles), Si (indigo downward triangles), Ca (purple asterisks), and Ni (pink diamonds) for both CL13 and LC18.

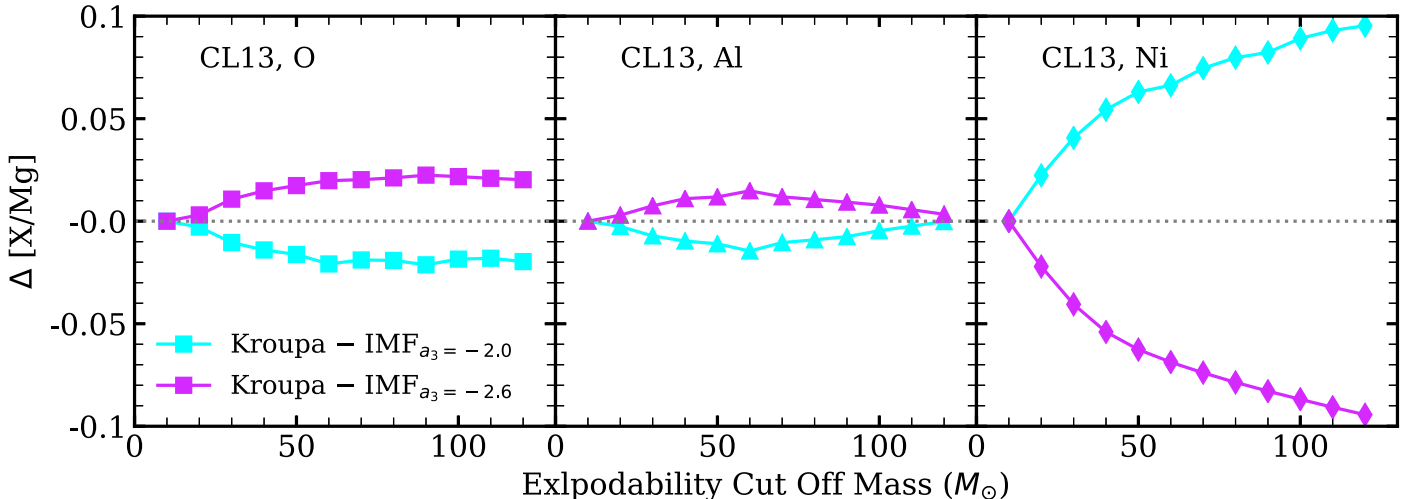


Figure 22. Theoretical $[X/Mg]$ abundance changes between the standard Kroupa IMF ($a_3 = -2.3$) and a Kroupa IMF with an altered high-mass slope as a function of changing explodability cutoff mass for O (left; squares), Al (middle; triangles), and Ni (right; diamonds). Abundance changes for $a_3 = -2.0$ are shown in cyan, and those for $a_3 = -2.6$ are shown in magenta. Net yields from CL13 are used.

Table 4
VICE Integrated Yields (Left) and [X/Mg] Abundances (Right) for Net CL13 Yields with [Fe/H] = 0.0, Exploding Stars Up to $30 M_{\odot}$

	Yield (M_{\odot}/M_{\odot} formed)			[X/Mg]		
	$a_3 = -2.0$	Kroupa	$a_3 = -2.6$	$a_3 = -2.0$	Kroupa	$a_3 = -2.6$
Fe	1.09E-03	6.85E-04	3.48E-04	-0.015	0.017	0.049
O	8.22E-03	4.66E-03	2.15E-03	0.214	0.204	0.193
Na	5.47E-05	3.10E-05	1.43E-05	0.329	0.318	0.307
Al	7.86E-05	4.50E-05	2.09E-05	0.208	0.201	0.195
Si	1.09E-03	6.51E-04	3.17E-04	0.273	0.285	0.297
P	5.59E-06	3.29E-06	1.58E-06	0.039	0.045	0.052
S	4.12E-04	2.47E-04	1.20E-04	0.181	0.194	0.208
K	4.78E-07	2.81E-07	1.35E-07	-0.750	-0.744	-0.738
Ca	5.30E-05	3.19E-05	1.56E-05	-0.025	-0.010	0.004
V	1.94E-07	1.18E-07	5.89E-08	-0.157	-0.136	-0.113
Cr	1.47E-05	8.93E-06	4.42E-06	0.005	0.023	0.044
Mn	8.66E-06	5.29E-06	2.65E-06	-0.039	-0.018	0.007
Co	3.65E-06	2.18E-06	1.08E-06	-0.004	0.008	0.029
Ni	1.09E-04	7.08E-05	3.73E-05	0.243	0.291	0.338
Cu	3.12E-07	1.75E-07	8.02E-08	-0.306	-0.320	-0.334

Note. All APOGEE elements but Ce are reported for all three IMFs investigated above.

Table 5
Same as Table 4 but for LC18 with Net Explosive Yields for Stars Up to $25 M_{\odot}$

	Yield (M_{\odot}/M_{\odot} formed)			[X/Mg]		
	$a_3 = -2.0$	Kroupa	$a_3 = -2.6$	$a_3 = -2.0$	Kroupa	$a_3 = -2.6$
Fe	7.24E-04	4.57E-04	2.34E-04	-0.103	-0.077	-0.050
O	5.96E-03	3.54E-03	1.71E-03	0.166	0.166	0.166
Na	3.65E-05	2.13E-05	1.01E-05	0.245	0.237	0.229
Al	4.94E-05	2.93E-05	1.41E-05	0.098	0.097	0.097
Si	8.51E-04	5.27E-04	2.65E-04	0.257	0.275	0.293
P	6.73E-06	4.11E-06	2.04E-06	0.212	0.224	0.237
S	3.14E-04	1.95E-04	9.89E-05	0.155	0.175	0.196
K	7.36E-07	4.48E-07	2.22E-07	-0.470	-0.460	-0.449
Ca	4.20E-05	2.63E-05	1.34E-05	-0.034	-0.011	0.012
V	1.20E-07	7.50E-08	3.80E-08	-0.273	-0.252	-0.230
Cr	8.11E-06	5.09E-06	2.60E-06	-0.163	-0.139	-0.115
Mn	4.50E-06	2.81E-06	1.43E-06	-0.232	-0.210	-0.188
Co	3.14E-06	1.92E-06	9.52E-07	0.022	0.034	0.046
Ni	6.67E-05	4.21E-05	2.16E-05	0.120	0.147	0.173
Cu	7.45E-07	4.36E-07	2.07E-07	0.164	0.157	0.150
Ce	1.71E-10	1.00E-10	4.76E-11	-1.209	-1.215	-1.222

Note. All APOGEE elements are reported.

and LC18. In the CL13 yields, we see that while Mg has an obvious mass dependence, the α -elements (O, Si, and Ca) and light odd-Z element (Al) track Mg and thus have little mass dependence in X/Mg. This explains our findings in Figure 13, where all four elements show small $\Delta[X/Mg]$ for a changing IMF. The Ni/Mg yields steeply decrease with stellar mass, causing larger changes in the [Ni/Mg] values when the IMF is varied.

While CL13 reported yields for all massive stars, LC18 publish their set R yields, where stars above $25 M_{\odot}$ are assumed to collapse to a black hole. Figure 21 plots their M set, which imposes the same mass cut as set R but explodes stars to $120 M_{\odot}$. These yields show very similar mass dependence to CL13. While O/Mg and Al/Mg do not vary much, Si, Ca, and Ni yields decrease with respect to Mg between 8 and $30 M_{\odot}$. The Ni/Mg yields drop the most but are shallower than CL13, suggesting a smaller IMF-induced abundance

change than that seen in Figure 13. We have only chosen to plot a few select elements in these figures, but integrated net yields for all APOGEE elements can be found in Tables 4 (CL13) and 5 (LC18).

The predicted abundance variability with changing IMF discussed in Section 5 employs net yields for [Fe/H] = 0 and explodes stars up to a birth mass of $30 M_{\odot}$. These choices impact the scale of the theoretical $\Delta[X/Mg]$ values. To explore the full range of possible $\Delta[X/Mg]$, we repeat our calculations for different explosibility cutoffs and metallicities. Figure 22 plots the $\Delta[X/Mg]$ values for the $a_3 = -2.0$ and -2.6 cases as we change the cutoff mass for O, Al, and Ni for the CL13 yields. A given mass on the x -axis indicates that all stars with progenitor masses $\leq M$ explode and contribute to nucleosynthesis, while those above do not. The $\Delta[O/Mg]$ and $\Delta[Al/Mg]$ values remain small (<0.03), with $\Delta[O/Mg]$ increasing to a plateau around ± 0.025 and $\Delta[Al/Mg]$ peaking near ± 0.02 for

a cutoff mass of $\sim 60 M_{\odot}$. The $\Delta[\text{Ni}/\text{Mg}]$ values are much more dependent on the cutoff mass, growing to $\sim \pm 0.1$ as we include stars approaching $120 M_{\odot}$. This limit gives an upper bound on the possible observable abundance changes induced by a changing IMF high-mass slope. We also investigate how changing the metallicity affects the $\Delta[X/\text{Mg}]$ values for the LC18 yield, which are calculated for $[\text{Fe}/\text{H}] = -3.0, -2.0, -1.0,$ and 0.0 . We find that the differences as a function of metallicity are smaller than those caused by the explosion mass cutoff, so we do not report them here. We will explore the impact of more complex explodability landscapes (Pejcha & Thompson 2015; Sukhbold et al. 2016) in future work.

ORCID iDs

Emily Griffith  <https://orcid.org/0000-0001-9345-9977>
 David H. Weinberg  <https://orcid.org/0000-0001-7775-7261>
 Jennifer A. Johnson  <https://orcid.org/0000-0001-7258-1834>
 Rachael Beaton  <https://orcid.org/0000-0002-1691-8217>
 D. A. García-Hernández  <https://orcid.org/0000-0002-1693-2721>
 Sten Hasselquist  <https://orcid.org/0000-0001-5388-0994>
 Jon Holtzman  <https://orcid.org/0000-0002-9771-9622>
 James W. Johnson  <https://orcid.org/0000-0002-6534-8783>
 Henrik Jönsson  <https://orcid.org/0000-0002-4912-8609>
 David M. Nataf  <https://orcid.org/0000-0001-5825-4431>
 Alexandre Roman-Lopes  <https://orcid.org/0000-0002-1379-4204>

References

- Ahumada, R., Allende Prieto, C., Almeida, A., et al. 2020, *ApJS*, 249, 3
 Andrews, B. H., Weinberg, D. H., Schönrich, R., & Johnson, J. A. 2017, *ApJ*, 835, 224
 Arlandini, C., Käppeler, F., Wisshak, K., et al. 1999, *ApJ*, 525, 886
 Asplund, M., Grevesse, N., Sauval, A. J., & Scott, P. 2009, *ARA&A*, 47, 481
 Astropy Collaboration, Price-Whelan, A. M., Sipőcz, B. M., et al. 2018, *AJ*, 156, 123
 Astropy Collaboration, Robitaille, T. P., Tollerud, E. J., et al. 2013, *A&A*, 558, A33
 Ballero, S. K., Matteucci, F., Origlia, L., & Rich, R. M. 2007, *A&A*, 467, 123
 Battistini, C., & Bensby, T. 2016, *A&A*, 586, A49
 Bensby, T., Feltzing, S., Gould, A., et al. 2017, *A&A*, 605, A89
 Bensby, T., Feltzing, S., & Lundström, I. 2003, *A&A*, 410, 527
 Bensby, T., Feltzing, S., & Oey, M. S. 2014, *A&A*, 562, A71
 Bensby, T., Yee, J. C., Feltzing, S., et al. 2013, *A&A*, 549, A147
 Bisterzo, S., Travaglio, C., Gallino, R., Wiescher, M., & Käppeler, F. 2014, *ApJ*, 787, 10
 Blanton, M. R., Bershady, M. A., Abolfathi, B., et al. 2017, *AJ*, 154, 28
 Bovy, J., Leung, H. W., Hunt, J. A. S., et al. 2019, *MNRAS*, 490, 4740
 Bovy, J., Rix, H.-W., Schlafly, E. F., et al. 2016, *ApJ*, 823, 30
 Bowen, I. S., & Vaughan, A. H. J. 1973, *ApOpt*, 12, 1430
 Chieffi, A., & Limongi, M. 2013, *ApJ*, 764, 21
 Cunha, K., & Smith, V. V. 2006, *ApJ*, 651, 491
 Das, P., Hawkins, K., & Jofré, P. 2020, *MNRAS*, 493, 5195
 De Silva, G. M., Freeman, K. C., Bland-Hawthorn, J., et al. 2015, *MNRAS*, 449, 2604
 Delgado Mena, E., Tsantaki, M., Adibekyan, V. Z., et al. 2017, *A&A*, 606, A94
 Duong, L., Asplund, M., Nataf, D. M., Freeman, K. C., & Ness, M. 2019a, *MNRAS*, 486, 5349
 Duong, L., Asplund, M., Nataf, D. M., et al. 2019b, *MNRAS*, 486, 3586
 Forsberg, R., Jönsson, H., Ryde, N., & Matteucci, F. 2019, *A&A*, 631, A113
 Fuhrmann, K. 1998, *A&A*, 338, 161
 Fulbright, J. P., McWilliam, A., & Rich, R. M. 2007, *ApJ*, 661, 1152
 Gallino, R., Arlandini, C., Busso, M., et al. 1998, *ApJ*, 497, 388
 García Pérez, A. E., Allende Prieto, C., Holtzman, J. A., et al. 2016, *AJ*, 151, 144
 Gilmore, G., Randich, S., Asplund, M., et al. 2012, *Msngr*, 147, 25
 Gravity Collaboration, Abuter, R., Amorim, A., et al. 2019, *A&A*, 625, L10
 Grevesse, N., Asplund, M., & Sauval, A. J. 2007, *SSRv*, 130, 105
 Grieco, V., Matteucci, F., Pipino, A., & Cescutti, G. 2012, *A&A*, 548, A60
 Grieco, V., Matteucci, F., Ryde, N., Schultheis, M., & Uttenthaler, S. 2015, *MNRAS*, 450, 2094
 Griffith, E., Johnson, J. A., & Weinberg, D. H. 2019, *ApJ*, 886, 84
 Gunn, J. E., Siegmund, W. A., Mannery, E. J., et al. 2006, *AJ*, 131, 2332
 Hawkins, K., Masseron, T., Jofré, P., et al. 2016, *A&A*, 594, A43
 Hayden, M. R., Bovy, J., Holtzman, J. A., et al. 2015, *ApJ*, 808, 132
 Hill, V., Lecœur, A., Gómez, A., et al. 2011, *A&A*, 534, A80
 Holtzman, J. A., Hasselquist, S., Shetrone, M., et al. 2018, *AJ*, 156, 125
 Holtzman, J. A., Shetrone, M., Johnson, J. A., et al. 2015, *AJ*, 150, 148
 Horta, D., Schiavon, R. P., Mackereth, J. T., et al. 2021, *MNRAS*, 500, 1385
 Johnson, C. I., Rich, R. M., Kobayashi, C., Kunder, A., & Koch, A. 2014, *AJ*, 148, 67
 Johnson, J. A. 2019, *Sci*, 363, 474
 Johnson, J. W., & Weinberg, D. H. 2020, *MNRAS*, 498, 1364
 Jönsson, H., Holtzman, J. A., Allende Prieto, C., et al. 2020, *AJ*, 160, 120
 Jönsson, H., Ryde, N., Schultheis, M., & Zoccali, M. 2017, *A&A*, 598, A101
 Kroupa, P. 2001, *MNRAS*, 322, 231
 Lecœur, A., Hill, V., Zoccali, M., et al. 2007, *A&A*, 465, 799
 Leung, H. W., & Bovy, J. 2019, *MNRAS*, 489, 2079
 Lian, J., Zasowski, G., Hasselquist, S., et al. 2020, *MNRAS*, 497, 3557
 Lian, J., Zasowski, G., Hasselquist, S., et al. 2021, *MNRAS*, 500, 282
 Limongi, M., & Chieffi, A. 2018, *ApJS*, 237, 13
 Lomaeva, M., Jönsson, H., Ryde, N., Schultheis, M., & Thorsbro, B. 2019, *A&A*, 625, A141
 Majewski, S. R., Schiavon, R. P., Frinchaboy, P. M., et al. 2017, *AJ*, 154, 94
 Martell, S. L., Sharma, S., Buder, S., et al. 2017, *MNRAS*, 465, 3203
 Masseron, T., García-Hernández, D. A., Santoveña, R., et al. 2020, *NatCo*, 11, 3759
 McWilliam, A., & Rich, R. M. 1994, *ApJS*, 91, 749
 Meléndez, J., Asplund, M., Alves-Brito, A., et al. 2008, *A&A*, 484, L21
 Ness, M., & Freeman, K. 2016, *PASA*, 33, e022
 Nidever, D. L., Holtzman, J. A., Allende Prieto, C., et al. 2015, *AJ*, 150, 173
 Osorio, Y., Allende Prieto, C., Hubeny, I., Mészáros, S., & Shetrone, M. 2020, *A&A*, 637, A80
 Pejcha, O., & Thompson, T. A. 2015, *ApJ*, 801, 90
 Prochaska, J. X., Naumov, S. O., Carney, B. W., McWilliam, A., & Wolfe, A. M. 2000, *AJ*, 120, 2513
 Queiroz, A. B. A., Anders, F., Chiappini, C., et al. 2020, *A&A*, 638, A76
 Rojas-Arriagada, A., Zasowski, G., Schultheis, M., et al. 2020, *MNRAS*, 499, 1037
 Rojas-Arriagada, A., Zoccali, M., Schultheis, M., et al. 2019, *A&A*, 626, A16
 Rybizki, J., Just, A., & Rix, H.-W. 2017, *A&A*, 605, A59
 Salpeter, E. E. 1955, *ApJ*, 121, 161
 Santos-Peral, P., Recio-Blanco, A., de Laverny, P., Fernández-Alvar, E., & Ordenovic, C. 2020, *A&A*, 639, A140
 Schultheis, M., Rojas-Arriagada, A., García Pérez, A. E., et al. 2017, *A&A*, 600, A14
 Sukhbold, T., Ertl, T., Woosley, S. E., Brown, J. M., & Janka, H. T. 2016, *ApJ*, 821, 38
 Vincenzo, F., Weinberg, D. H., & Miglio, A. 2021, arXiv:2101.04488
 Weinberg, D. H., Holtzman, J. A., Hasselquist, S., et al. 2019, *ApJ*, 874, 102
 Wilson, J. C., Hearty, F. R., Skrutskie, M. F., et al. 2019, *PASP*, 131, 055001
 Zasowski, G., Cohen, R. E., Chojnowski, S. D., et al. 2017, *AJ*, 154, 198
 Zasowski, G., Schultheis, M., Hasselquist, S., et al. 2019, *ApJ*, 870, 138